

# Triangularity and Dipole Asymmetry in Heavy Ion Collisions

Derek Teaney and Li Yan

*Department of Physics and Astronomy,  
Stony Brook University, Stony Brook,  
New York 11794-3800, United States*

(Dated: October 22, 2018)

## Abstract

We introduce a cumulant expansion to parameterize possible initial conditions in relativistic heavy ion collisions. We show that the cumulant expansion converges and that it can systematically reproduce the results of Glauber type initial conditions. At third order in the gradient expansion, the cumulants characterize the triangularity  $\langle r^3 \cos 3(\phi - \psi_{3,3}) \rangle$  and the dipole asymmetry  $\langle r^3 \cos(\phi - \psi_{1,3}) \rangle$  of the initial entropy distribution. We show that for mid-peripheral collisions the orientation angle of the dipole asymmetry  $\psi_{1,3}$  has a 20% preference out of plane. This leads to a small net  $v_1$  out of plane. In peripheral and mid-central collisions the orientation angles  $\psi_{1,3}$  and  $\psi_{3,3}$  are strongly correlated, but this correlation disappears towards central collisions. We study the ideal hydrodynamic response to these cumulants and determine the associated  $v_1/\epsilon_1$  and  $v_3/\epsilon_3$  for a massless ideal gas equation of state. The space time development of  $v_1$  and  $v_3$  is clarified with figures. These figures show that  $v_1$  and  $v_3$  develop towards the edge of the nucleus, and consequently the final spectra are more sensitive to the viscous dynamics of freezeout. The hydrodynamic calculations for  $v_3$  are provisionally compared to Alver and Roland fit of STAR inclusive two particle correlation functions. Finally, we propose to measure the  $v_1$  associated with the dipole asymmetry and the correlations between  $\psi_{1,3}$  and  $\psi_{3,3}$  by measuring a two particle correlation with respect to the participant plane,  $\langle \cos(\phi_\alpha - 3\phi_\beta + 2\Psi_{PP}) \rangle$ . The hydrodynamic prediction for this correlation function is several times larger than a correlation currently measured by the STAR collaboration,  $\langle \cos(\phi_\alpha + \phi_\beta - 2\Psi_{PP}) \rangle$ . This experimental measurement would provide convincing evidence for the hydrodynamic and geometric interpretation of two particle correlations at RHIC.

## I. INTRODUCTION

In a recent and significant paper B. Alver and G. Roland (AR) [1] provided the most compelling explanation to date for the striking features measured in two particle correlations at the Relativistic Heavy Ion Collider [2–7]. These features (which are described with picturesque names such as the “ridge” and “shoulder”) are said to arise from the collective response to fluctuating initial conditions. Specifically, if the initial conditions are parameterized with a quadrupole and triangular moment, the two particle correlations reflect the response of the nuclear medium to these anisotropies. The work of AR was motivated in part by event by event simulations of heavy ion collisions with ideal hydrodynamics which showed that the flow from fluctuating initial conditions can describe the general features of the measured two particle correlations [8]. The general idea that the curious correlations are due to a third harmonic in the flow profile was previously suggested by Sorensen [9]. In addition, many of the features of the observed two particle correlations were found in the AMPT model [10–12], though the geometric nature of these correlations was not understood before the work of Alver and Roland.

The hydrodynamic interpretation of the measured two particle correlations is important for several reasons. First, before this conclusion there was a significant correlation between the measured particles which was not understood. This confusion casted doubt on the hydrodynamic interpretation of RHIC results and clouded the important conclusion that the shear viscosity to entropy ratio of QCD is of order  $\sim \hbar/4\pi$  near the phase transition [13]. However, since the unusual two particle correlations are actually a prediction of hydrodynamics, the observation of these unusual features in the data validates hydrodynamics as an appropriate effective theory for heavy ion events and marginalizes other models. Further, once the hydrodynamic interpretation is adopted the measured correlations can be used to constrain the properties of the medium, *e.g.* the shear viscosity and the Equation of State (EOS). In particular the effect of viscosity was calculated in Refs. [14, 15] which will be discussed more completely below.

Motivated by these results, the current work will characterize the fluctuating initial conditions with a cumulant expansion. Instead of running hydrodynamics event to event, the linear response to specified cumulants can be calculated with ideal or viscous hydrodynamics. Subsequently, these response functions can be combined with a Glauber model for the event-by-event cumulants (and their correlations), and the combined result can be fairly compared to data. At third order in the gradient expansion, the initial condition is parameterized by a radial dependence to the dipole moment,  $\langle r^3 \cos \phi \rangle$ , and the triangularity,  $\langle r^3 \cos 3\phi \rangle$ . In Section III we will calculate (with ideal hydrodynamics) how the medium responds to these moments and illustrate how this response develops in space and time. Subsequently in Section IV we will compute the corresponding particle spectra  $v_1(p_T)$  and  $v_3(p_T)$  and study the sensitivity to certain model parameters related to freezeout. In Section V A we will make a comparison to  $V_{3\Delta}/V_{2\Delta}$  as extracted by Alver and Roland in their analysis of two particle correlations. We will also make definite predictions for the dipole asymmetry  $v_1(p_T)$ , which, if confirmed, would firmly establish the geometric nature of the two particle correlations. The comparison to data is not final as the effects of resonance decays, viscosity, and higher

cumulants have not been included, Nevertheless, the preliminary comparison will firmly tie the formal cumulant expansion outlined in this paper to the measured correlations. Finally, we will compare our calculations to the recent results of Refs. [14–16] in Section V B.

## II. CUMULANT EXPANSION AND HYDRODYNAMICS AT RHIC

### A. The initial conditions for ideal hydrodynamics

In this paper we will use 2+1 dimensional boost invariant ideal hydrodynamics to simulate RHIC events [13, 17, 18]. Briefly, in ideal hydrodynamics the stress tensor satisfies the constituent relation and the conservation laws:

$$T^{\mu\nu} = (e + \mathcal{P}(e))u^\mu u^\nu + \mathcal{P}(e)g^{\mu\nu}, \quad \nabla_\mu T^{\mu\nu} = 0, \quad (2.1)$$

where  $e$  is the energy density,  $u^\mu$  is the flow velocity, and the pressure  $\mathcal{P}$  is specified by the EOS,  $\mathcal{P} = \mathcal{P}(e)$ . We will work in flat space but with coordinates

$$\tau = \sqrt{t^2 - z^2}, \quad \eta_s = \frac{1}{2} \log \left( \frac{t+z}{t-z} \right).$$

With the assumption of boost invariance, the hydrodynamic fields are independent of  $\eta_s$  and  $u^\eta = 0$ . Using the constraint  $u_\mu u^\mu = -1$ , the independent fields which must be determined by solving the conservation laws are

$$e(\tau, \mathbf{x}), \quad u^x(\tau, \mathbf{x}) \quad u^y(\tau, \mathbf{x}), \quad (2.2)$$

where  $\mathbf{x}$  denotes two dimensional vectors in the transverse plane. We will specify the initial conditions for the subsequent evolution in what follows. At the initial time  $\tau_o$  it is reasonable to assume that flow fields are small,  $u^x \simeq u^y \simeq 0$ . This leaves the initial energy density which must be specified  $e(\tau_o, x, y)$ . We will specify the initial entropy density  $s(\tau_o, x, y)$  with a cumulant expansion and infer the initial energy density from the equation of state.

A typical initial condition might be fairly complicated involving several structures. However, the effect of the shear viscosity is to damp the highest Fourier modes. Thus, after damping the shortest wavelengths, the initial entropy distribution is approximately described by a Gaussian with average squared radius  $\langle r^2 \rangle$  and elliptic eccentricity  $\epsilon_2$  as has traditionally been used to characterize heavy ion events [17]. The damping of the highest Fourier modes is nicely seen in Fig. 1 of a recent preprint [15]. The next paragraphs formalize this description and categorize corrections.

### B. Cumulants

The Fourier transform of the entropy density for a given initial condition is

$$\int d^2\mathbf{x} e^{i\mathbf{k}\cdot\mathbf{x}} \rho(x) = \rho(\mathbf{k}), \quad (2.3)$$

where  $\rho(\mathbf{x}) = \tau_o s(\tau_o, \mathbf{x})/S_{\text{tot}}$  and  $S_{\text{tot}} = \int \tau_o d^2\mathbf{x} s(\tau_o, \mathbf{x})$  is the total entropy per space time rapidity. Since the highest Fourier modes are damped, we will expand the initial distribution in  $\mathbf{k}$ . Expanding both sides of Eq. (2.3) with respect to  $\mathbf{k}$ ,

$$\rho(\mathbf{k}) = 1 + ik^a \rho_{1,a} + \frac{(ik^a)(ik^b)}{2!} \rho_{2,ab} + \dots, \quad (2.4)$$

we see that  $\rho(\mathbf{k})$  generates moments of the entropy distribution

$$\rho_{1,a} = \langle x_a \rangle, \quad \rho_{2,ab} = \langle x_a x_b \rangle, \quad (2.5)$$

where the average is appropriately defined

$$\langle \dots \rangle = \int d^2\mathbf{x} \rho(\mathbf{x}) \dots. \quad (2.6)$$

Although we could classify the initial conditions with these moments, a cumulant expansion seems more natural since the average Glauber distribution is roughly Gaussian and the cumulants are translationally invariant. We therefore define  $W(\mathbf{k})$

$$\exp(W(\mathbf{k})) \equiv \int d^2\mathbf{x} e^{i\mathbf{k}\cdot\mathbf{x}} \rho(\mathbf{x}), \quad (2.7)$$

and expand both sides in a fourier series

$$W(\mathbf{k}) = 1 + ik^a W_{1,a} + \frac{1}{2!} (ik^a)(ik^b) W_{2,ab} + \dots. \quad (2.8)$$

From this expansion we see that  $W(\mathbf{k})$  is the generating function of cumulants of the underlying distribution  $\rho(\mathbf{k})$

$$W_{1,l} = \langle x_l \rangle, \quad W_{2,ab} = \langle x_a x_b \rangle - \langle x_a \rangle \langle x_b \rangle. \quad (2.9)$$

From now on we will shift the origin so that  $\langle x_a \rangle = 0$ , and the distribution is approximately Gaussian to quadratic order

$$\rho(\mathbf{k}) = \exp\left(-\frac{1}{2} k^a k^b W_{2,ab}\right). \quad (2.10)$$

Higher order corrections in this expansion will correct the distribution away from the Gaussian. The tensor  $W_{2,ab}$  is a reducible tensor and should be decomposed into irreducible components,

$$W_{2,ab} = \frac{1}{2} W_{2,cc} \delta_{ab} + \left( W_{2,ab} - \frac{1}{2} W_{2,cc} \delta_{ab} \right). \quad (2.11)$$

We orient the  $x, y$  axes to the participant plane [19] where  $W_{2,xy} = 0$ . Then the irreducible moments are

$$W_{2,aa} = \langle x^2 + y^2 \rangle, \quad (2.12)$$

$$W_{2,xx} - \frac{1}{2} W_{2,cc} \delta_{xx} = \frac{1}{2} \langle x^2 - y^2 \rangle. \quad (2.13)$$

Clearly the irreducible components of the cumulant expansion are related to the traditional parameters of heavy ion physics:

$$\langle x^2 + y^2 \rangle, \quad \text{and} \quad \epsilon_2 \equiv \frac{\langle y^2 - x^2 \rangle}{r^2}. \quad (2.14)$$

To write down corrections to these results it is more convenient and illustrative to use cylindrical tensors rather than Cartesian tensors. Appendix A develops this expansion in detail and only certain features will be summarized here. Appendix A 1 expands  $W(\mathbf{k})$  in a Fourier series:

$$W(\mathbf{k}) = W_0(k) + 2 \sum_{n=1}^{\infty} W_n^c(k) \cos(n\phi_k) + 2 \sum_{n=1}^{\infty} W_n^s(k) \sin(n\phi_k), \quad (2.15)$$

where  $k$  and  $\phi_k$  are the norm and azimuthal angle of the momentum vector. The  $W_n^{c,s}(k)$  are also expanded in  $k$  to characterize the distribution at largest wavelength:

$$W_0(k) = \frac{1}{2!} W_{0,2}(ik)^2 + O(k^4), \quad (2.16a)$$

$$W_1^c(k) = W_{1,1}^c + O(k^3), \quad (2.16b)$$

$$W_1^s(k) = W_{1,1}^s + O(k^3), \quad (2.16c)$$

$$W_2^c(k) = \frac{1}{2!} W_{2,2}^c(ik)^2 + O(k^4), \quad (2.16d)$$

$$W_2^s(k) = W_{2,2}^s + O(k^4). \quad (2.16e)$$

After Appendix A we find that to order  $k^2$

$$W_{0,2} = \frac{1}{2} \langle r^2 \rangle, \quad (2.17)$$

$$W_{1,1}^c = 0, \quad (2.18)$$

$$W_{1,1}^s = 0, \quad (2.19)$$

$$W_{2,2}^c = \frac{1}{4} \langle r^2 \cos(2\phi) \rangle, \quad (2.20)$$

$$W_{2,2}^s = 0. \quad (2.21)$$

Here we have used translational invariance and rotational invariance (as in the Cartesian case) to eliminate  $W_{1,1}^c$ ,  $W_{1,1}^s$ , and  $W_{2,2}^s$ . To third order in the gradient expansion the dipole terms  $W_1^c(k)$  and  $W_1^s(k)$  are non-zero

$$W_1^c(k) = \frac{1}{3!} W_{1,3}(ik)^3 + O(k^5), \quad W_{1,3} = \frac{3}{8} \langle r^3 \cos \phi \rangle, \quad (2.22a)$$

$$W_1^s(k) = \frac{1}{3!} W_{1,3}(ik)^3 + O(k^5), \quad W_{1,3} = \frac{3}{8} \langle r^3 \sin \phi \rangle. \quad (2.22b)$$

Similarly, at third order in the gradient expansion there are terms proportional to  $\cos(3\phi)$

$$W_3^c(k) = \frac{1}{3!} W_{3,3}(ik)^3 + O(k^5), \quad W_{3,3}^c = \frac{1}{8} \langle r^3 \cos(3\phi) \rangle, \quad (2.22c)$$

$$W_3^s(k) = \frac{1}{3!} W_{3,3}(ik)^3 + O(k^5), \quad W_{3,3}^s = \frac{1}{8} \langle r^3 \sin(3\phi) \rangle. \quad (2.22d)$$

Once the fourier coefficients  $W_{n,m}$  are specified, the entropy distribution in space can be found with a fourier transform; see Eqs. 2.34 and 2.35 and the surrounding text for further discussion.

### C. A strategy for event by event hydrodynamics

If the cumulants beyond second order are in some sense small, then the change in the hydrodynamic spectra due to a specified set of higher cumulants is linearly proportional to the deformation

$$\frac{d\delta N}{d\phi_p} = \sum_{n,m,\{s,c\}} \left[ \frac{1}{W_{n,m}^{c,s}} \frac{d\delta N}{d\phi_p} \right]_{n,m,\{s,c\}} W_{n,m}^{c,s}, \quad (2.23)$$

where

$$\left[ \frac{1}{W_{n,m}^{c,s}} \frac{d\delta N}{d\phi_p} \right]_{n,m,\{c,s\}}, \quad (2.24)$$

is the normalized response to a given cumulant. If the non-linear interactions between the elliptic flow and the higher cumulants can be ignored (*i.e.* the elliptic flow is sufficiently small), then the background Gaussian is approximately radially symmetric and the response of the sin terms are related to the response of the cosine terms through a rotation. In this case, we are free to rotate our coordinate system by an angle  $\psi_{n,m}$

$$\psi_{n,m} = \frac{1}{n} \text{atan2}(W_{n,m}^s, W_{n,m}^c) + \frac{\pi}{n}, \quad (2.25)$$

so that the sin terms vanish. In this rotated frame (which we will notate as  $\hat{W}$ ) the cumulants are

$$\hat{W}_{n,m}^s = 0, \quad \hat{W}_{n,m}^c = -\sqrt{(W_{n,m}^c)^2 + (W_{n,m}^s)^2}, \quad (2.26)$$

and the spectrum can be written

$$\frac{d\delta N}{d\phi_p} = \sum_{n,m,c} \left[ \frac{1}{\hat{W}_{n,m}^c} \frac{d\delta N}{d(\phi_p - \psi_{n,m})} \right]_{n,m,\{c\}} \hat{W}_{n,m}^c. \quad (2.27)$$

Thus, the assumption of a rotationally invariant background reduces the number of coefficients by a factor of two.

In this paper we will assume that all deformations from spherical are small including the elliptic flow. Thus, we will neglect the non-linear couplings between the elliptic flow and the triangular flow and the elliptic flow and the dipolar flow. We have investigated the influence of the ellipticity on the triangular and dipolar flow and our preliminary findings show that the effect of the elliptic flow on the triangular flow is small. A similar finding was reported in the very recent preprint by the Duke group [20]. However, the effect of the elliptic flow on the dipolar flow is non-negligible when the dipole angle is oriented in plane. This complication will be reported on in future work [21].

The angle  $\psi_{2,2}$  specifies the orientation of the participant plane  $\Psi_{PP}$ , and the second order cumulant  $\hat{W}_{2,2}^c$  determines the ellipticity

$$\epsilon_2 \equiv -\frac{\langle r^2 \cos 2(\phi - \Psi_{PP}) \rangle}{\langle r^2 \rangle} = -\frac{4\hat{W}_{2,2}^c}{\langle r^2 \rangle}, \quad \Psi_{PP} \equiv \psi_{2,2}. \quad (2.28)$$

The participant plane angle  $\Psi_{PP}$  is distinct from the reaction plane angle which we denote with  $\Psi_R$ .

The third order cumulant  $\hat{W}_{3,3}^c$  describes the triangularity as introduced by Alver and Roland. These authors suggested a definition of the triangularity and orientation angle  $\epsilon_3^{AR}$  and  $\psi_3^{AR}$  with a quadratic radial weight

$$\epsilon_3^{AR} = -\frac{\langle r^2 \cos(3(\phi - \Psi_3^{AR})) \rangle}{\langle r^2 \rangle}, \quad \Psi_3^{AR} = \frac{1}{3} \text{atan2}(\langle r^2 \sin(3\phi) \rangle, \langle r^2 \cos(3\phi) \rangle) + \frac{\pi}{3}. \quad (2.29)$$

We will abandon this analytically frustrated definition, and define the triangularity  $\epsilon_3$  and the associated angle with an  $r^3$  weight

$$\epsilon_3 \equiv -\frac{\langle r^3 \cos 3(\phi - \psi_{3,3}) \rangle}{\langle r^3 \rangle} = -\frac{8\hat{W}_{3,3}^c}{\langle r^3 \rangle}, \quad (2.30)$$

$$\psi_{3,3} \equiv \frac{1}{3} \text{atan2}(\langle r^3 \sin 3\phi \rangle, \langle r^3 \cos 3\phi \rangle) + \frac{\pi}{3}. \quad (2.31)$$

The difference between the  $r^2$  and  $r^3$  weight is captured by the response of the system to the fifth order cumulants,  $W_{3,5}^c \propto [\langle r^5 \cos 3\phi \rangle - 4 \langle r^2 \rangle \langle r^3 \cos 3\phi \rangle]$ . Recent studies of the response of the system to  $\epsilon_5$  (or  $W_{5,5}$  in the current context) suggests that the response to these fifth order cumulants will be small [14].

The third order cumulant  $\hat{W}_{1,3}^c$  describes a dipole asymmetry and also appears to the same order in the gradient expansion. By analogy we define  $\epsilon_1$  and  $\psi_{1,3}$

$$\epsilon_1 \equiv -\frac{\langle r^3 \cos(\phi - \psi_{1,3}) \rangle}{\langle r^3 \rangle} = -\frac{8\hat{W}_{1,3}^c}{3\langle r^3 \rangle}, \quad (2.32)$$

$$\psi_{1,3} \equiv \text{atan2}(\langle r^3 \sin \phi \rangle, \langle r^3 \cos \phi \rangle) + \pi. \quad (2.33)$$

Estimates for these parameters and their correlations will be given in the next section.

#### D. The dipole asymmetry and triangularity

To get a feeling for the dipole asymmetry and triangularity we first record the explicit coordinate space expressions for a distribution with only triangularity

$$s(\mathbf{x}, \tau) \propto \left[ 1 + \frac{\langle r^3 \rangle \epsilon_3}{24} \left( \left( \frac{\partial}{\partial x} \right)^3 - 3 \left( \frac{\partial}{\partial y} \right)^2 \frac{\partial}{\partial x} \right) \right] e^{-\frac{r^2}{\langle r^2 \rangle}}, \quad (2.34)$$

and a distribution with only a dipole asymmetry

$$s(\mathbf{x}, \tau) \propto \left[ 1 + \frac{\langle r^3 \rangle \epsilon_1}{8} \left( \left( \frac{\partial}{\partial x} \right)^3 + \left( \frac{\partial}{\partial y} \right)^2 \frac{\partial}{\partial x} \right) \right] e^{-\frac{r^2}{\langle r^2 \rangle}}. \quad (2.35)$$

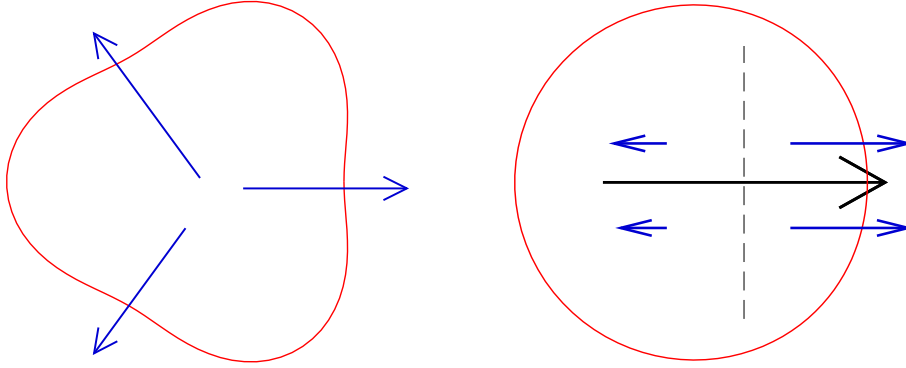


FIG. 1: A schematic of an event with (a) net triangularity and (b) net dipole asymmetry. The triangularity produces a net  $v_3(p_T)$  and the dipole asymmetry produces a net  $v_1(p_T)$ . The cross in (b) indicates the center of entropy (analogous to the center of mass) and the large arrow indicates the orientation of the dipole.

Here the orientation angles  $\psi_{3,3}$  and  $\psi_{1,3}$  are set to zero. At large enough radius the derivative terms become large and overwhelm the leading term making the distribution negative. This is an unavoidable consequence of truncating a cumulant expansion at any finite order. As explained in Appendix A we regulate these terms and adjust the overall constant to reproduce the total entropy in a central RHIC collision. Fig. 1a and Fig. 1b illustrate initial conditions with net triangularity and net dipole asymmetry respectively. The distribution with net triangularity leads to a  $v_3(p_T)$  while the dipole asymmetry leads to a  $v_1(p_T)$ .

To estimate these parameters and their correlations we have used the PHOBOS monte carlo Glauber code [22]. Fig. 2 shows the distribution of  $\epsilon_1$ ,  $\epsilon_2$  and  $\epsilon_3$  as a function of the number of participants. We see that the dipole asymmetry is about a factor of two smaller than the triangularity but is not negligibly small.

Fig. 3 shows the distribution of  $\psi_{1,3}$  and  $\psi_{3,3}$  with respect to reaction plane at various impact parameters. We see that although  $\psi_{3,3}$  is uncorrelated with respect to the reaction plane,  $\psi_{1,3}$  shows an anti-correlation with respect to the reaction plane, which eventually disappears toward central collisions.

More importantly, the angles  $\psi_{1,3}$  and  $\psi_{3,3}$  are strongly correlated in mid central collisions (a similar observation was made recently by Staig and Shuryak [23]). Fig. 4 shows the conditional probability distribution, *i.e.*

$$P(\psi_{3,3}|\psi_{1,3}, \Psi_R) \equiv \text{The probability of } \psi_{3,3} \text{ given } \psi_{1,3} \text{ and } \Psi_R.$$

The strong correlation may be explained physically as follows. When the dipole asymmetry is in plane then the triangular axis is at  $\pi/3$ , *i.e.* the point of the triangle is aligned with the dipole axis as exhibited in Fig. 5(a). However, when the dipole axis is out of plane then the triangular axis is also out of plane as exhibited in Fig. 5(b).

These correlations are a reflection of the almond shape geometry and their general form can be established by symmetry arguments. First, since the probability of finding a dipole asymmetry in a given quadrant of the ellipse is the same for every quadrant, the probability



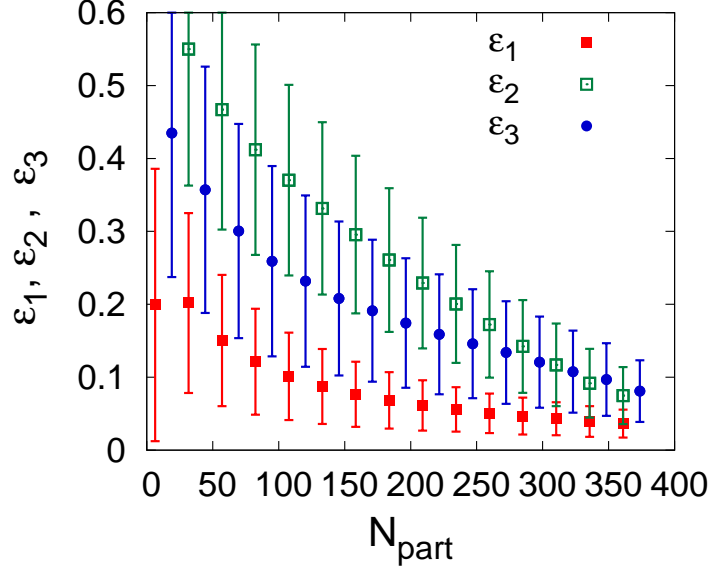


FIG. 2: Size of the moments  $\epsilon_1$ ,  $\epsilon_2$  and  $\epsilon_3$  as a function of the number of participants. The points indicate the average value of  $\langle\langle\epsilon_n\rangle\rangle$  and the errorbars indicate the variance of  $\epsilon_n$  at fixed  $N_{\text{part}}$ .

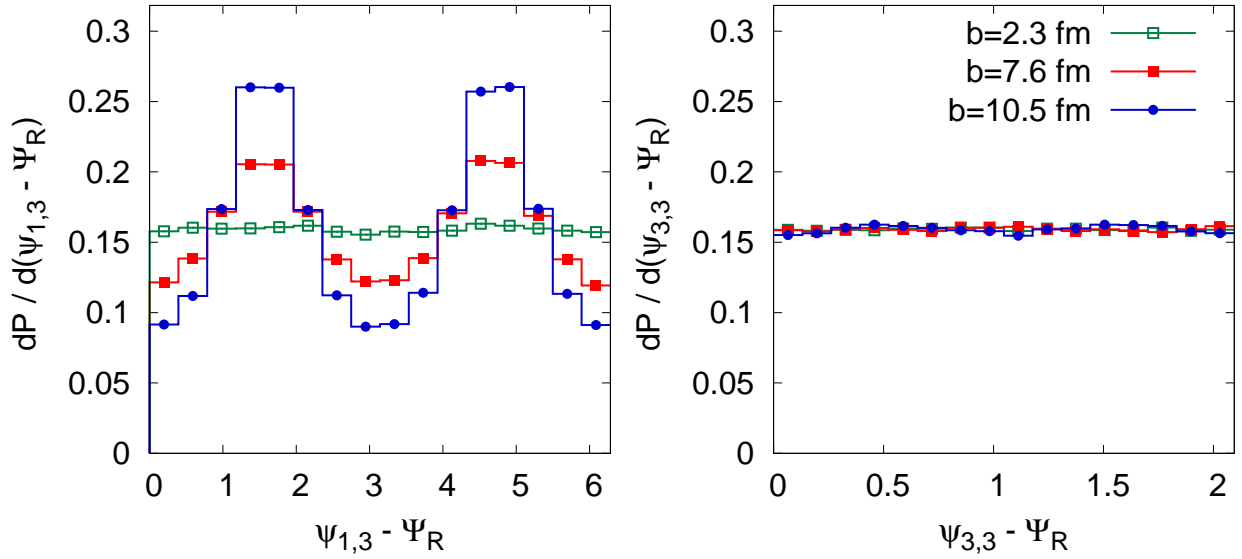


FIG. 3: Distribution of the angles  $\psi_{1,3}$  and  $\psi_{3,3}$  with respect to the reaction plane for three different impact parameters.

distributions  $dP/d(\psi_{1,3} - \Psi_R)$  must only involve even cosine terms

$$\frac{dP}{d\psi_{1,3}} = \frac{1}{2\pi} (1 - 2A \cos 2(\psi_{1,3} - \Psi_R)) + \dots \quad (2.36)$$

The sign has been chosen so that a positive  $A$  coefficient describes the out-of plane preference seen in Fig. 3. The coefficient  $A$  must vanish in a cylindrically symmetric collision, and for

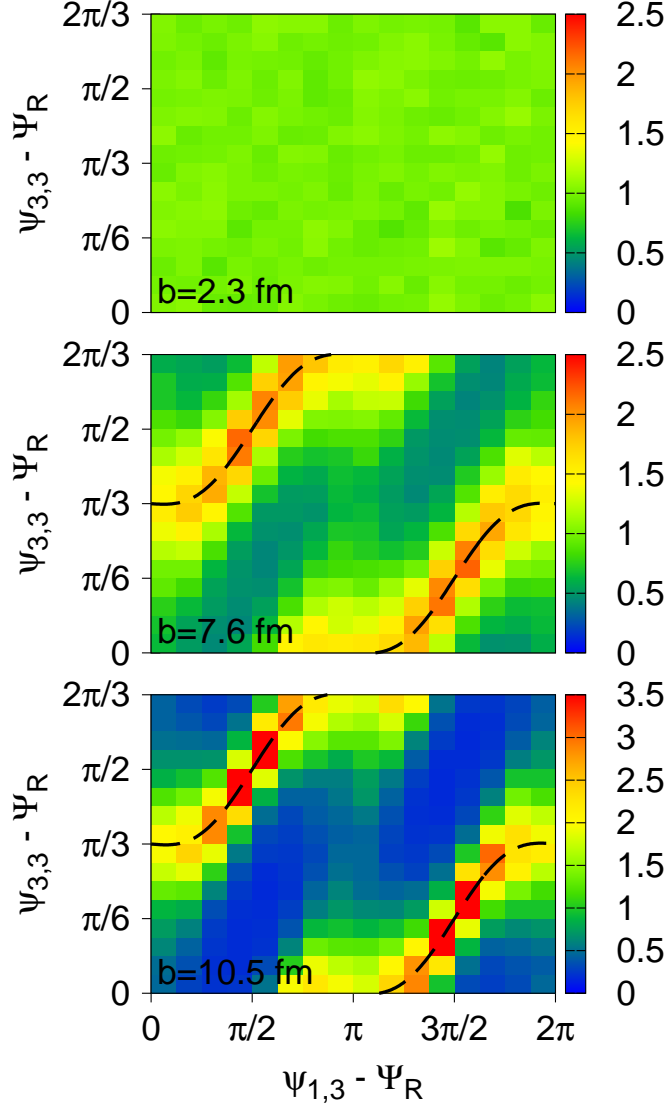


FIG. 4: The conditional probability distribution  $P(\psi_{3,3}|\psi_{1,3}\Psi_R)$  for three different impact parameters  $b = 0, 7.6, 10.5$  fm. The functional form of the dashed curve is given by Eq. (2.40) with fit parameter  $C = 0.53$  for  $b = 7.6$  fm and  $C = 0.56$  for  $b = 10.5$  fm.

small anisotropy we have

$$A \propto \langle\langle \epsilon_2 \rangle\rangle, \quad (2.37)$$

where the double brackets denotes an event averaged  $\epsilon_2$ . Similarly  $dP/d(\psi_{3,3} - \Psi_R)$  must involve even cosine terms and must be  $2\pi/3$  periodic

$$\frac{dP}{d(\psi_{3,3} - \Psi_R)} = \frac{1}{2\pi} (1 + 2A_6 \cos(6(\psi_{3,3} - \Psi_R)) + \dots). \quad (2.38)$$

The relatively high fourier number  $n = 6$  explains the smallness of the observed asymmetry, and  $A_6$  will be ignored from now on. The form of the conditional probability distribution can also be established based on general considerations. Appendix B uses symmetry arguments,

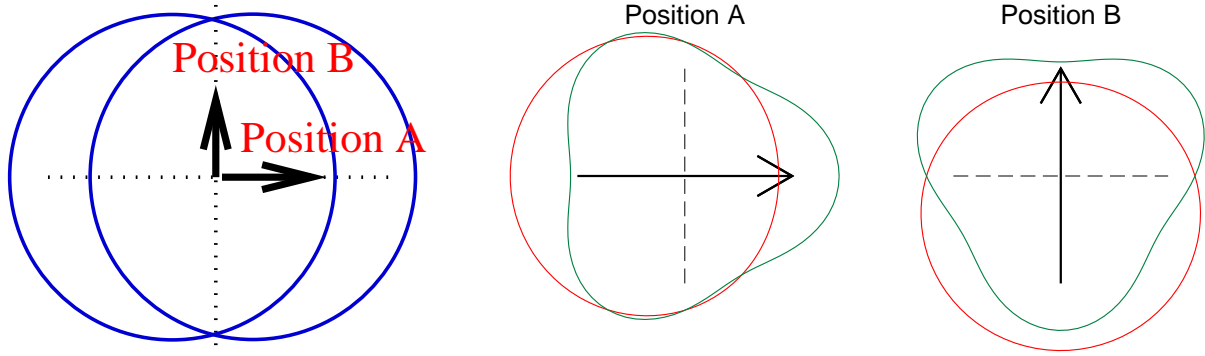


FIG. 5: The figure qualitatively describes the fluctuations associated with the Glauber model as illustrated in Fig. 4. When the dipole asymmetry is in plane (Position A), then the tip of triangularity is aligned with dipole asymmetry. When the dipole asymmetry is out of plane (Position B), the tip of the triangle is anti-aligned with the dipole asymmetry.

a fourier expansion, and the statement that the correlation is strongest when the triangle and dipole angles are aligned at  $\pi/2$  out of plane, to establish a three parameter functional form which describes the correlations fairly well

$$P(\psi_{3,3}|\psi_{1,3}, \Psi_R) = \frac{1}{2\pi} \left[ 1 - 2(B_0 - 2B_2 \cos(2\psi_{1,3} - 2\Psi_R)) \cos(3\psi_{3,3} - \phi^* - 2\Psi_R) \right], \quad (2.39)$$

where

$$\phi^* = \psi_{1,3} - C \sin(2\psi_{1,3} - 2\Psi_R). \quad (2.40)$$

The signs are chosen so that  $B_0$ ,  $B_2$ , and  $C$  are positive constants in the final fits. A sample fit with this functional form is given in Fig. 16 of Appendix B. The phase angle  $\phi^*$  is illustrated by the dashed black line in Fig. 4, which is found by solving  $3\psi_{3,3} - \phi^* + 2\Psi_R = \pi$  for  $\psi_{3,3}$ . Although we have written the conditional probability when the reaction plane angle is fixed, the same arguments could have been used to determine the functional form of the conditional probability when the participant plane angle is fixed, *i.e.*

$$P(\psi_{3,3}|\psi_{1,3}\Psi_{PP}) = \text{Eq. (2.39) with } \Psi_R \rightarrow \Psi_{PP} \text{ and slightly different numerical coefficients.} \quad (2.41)$$

In the limit of small elliptic eccentricity the coefficients scale as

$$B_0 \propto \langle\langle \epsilon_2 \rangle\rangle, \quad B_2 \propto \langle\langle \epsilon_2 \rangle\rangle^2, \quad C \propto \langle\langle \epsilon_2 \rangle\rangle, \quad (2.42)$$

as is shown in Appendix B. Thus the conditional probability distribution simplifies in this limit to

$$P(\psi_{3,3}|\psi_{1,3}\Psi_R) = \frac{1}{2\pi} [1 - 2B_0 \cos(3\psi_{3,3} - \psi_{1,3} - 2\Psi_R)], \quad (2.43)$$

which describes almost all of the essential physical features.

The strong correlation means that if the triangular and the participant planes are known, then the dipole plane can be determined statistically. The probability distribution of  $\psi_{1,3}$

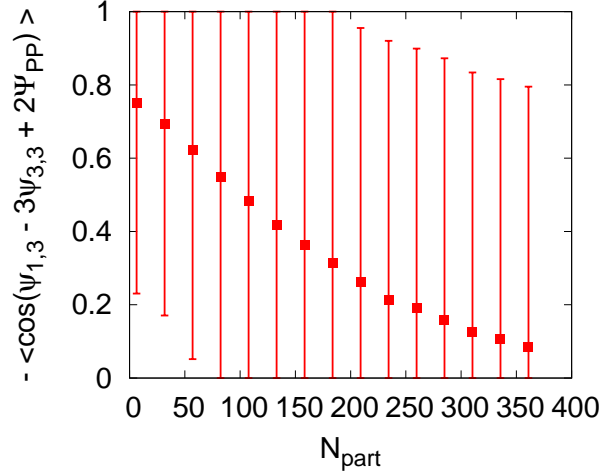


FIG. 6: Correlation of the true dipole angle  $\psi_{1,3}$  and the estimated event plane angle  $\psi_{1,3}^{\text{mp}} = 3\psi_{3,3} - 2\Psi_{PP} - \pi$ . The points indicate the average  $\langle\langle \cos(\psi_{1,3} - \psi_{1,3}^{\text{mp}}) \rangle\rangle$  and the errorbars indicate the variance of this quantity at fixed  $N_{\text{part}}$ .

for fixed  $\psi_{3,3}$  and  $\Psi_{PP}$  is approximately

$$P(\psi_{1,3}|\psi_{3,3}\Psi_{PP}) \simeq \frac{1}{2\pi} \left[ 1 + 2A \cos(2\psi_{1,3} - 2\Psi_{PP}) - 2B_0 \cos(3\psi_{3,3} - \psi_{1,3} - 2\Psi_{PP}) \right]. \quad (2.44)$$

Maximizing this probability we determine the most probable angle of  $\psi_{1,3}^{\text{mp}}$  given  $\psi_{3,3}$  and  $\Psi_{PP}$ . Neglecting the  $A$  coefficient which is significantly smaller than  $B_0$  we find

$$\psi_{1,3}^{\text{mp}} = 3\psi_{3,3} - 2\Psi_{PP} - \pi. \quad (2.45)$$

To estimate the degree of correlation between the most probable value and  $\psi_{1,3}$  we calculate

$$-\langle\langle \cos(\psi_{1,3} - 3\psi_{3,3} + 2\Psi_{PP}) \rangle\rangle, \quad (2.46)$$

and illustrate the result in Fig. 6. We will use this correlation in Section V A to make a definite prediction for the behavior of two particle correlations with respect to the reaction plane.

### E. Convergence of the cumulant expansion for smooth Glauber type initial conditions

In the previous section we introduced a cumulant expansion to characterize the response of the system to a set of perturbations. In this section we will study the convergence of the cumulant expansion. Specifically, for a smooth (optical) Glauber profile, we will replace the initial entropy distribution with an approximately Gaussian profile and cumulant corrections through fourth order. The distribution of entropy in the optical Glauber model (see Appendix A 2) is first used to calculate  $\langle r^2 \rangle$  and  $\langle r^2 \cos 2\phi \rangle$ , which determines the two coefficients of the Gaussian. Also the normalization (*i.e.* the total entropy) is the same

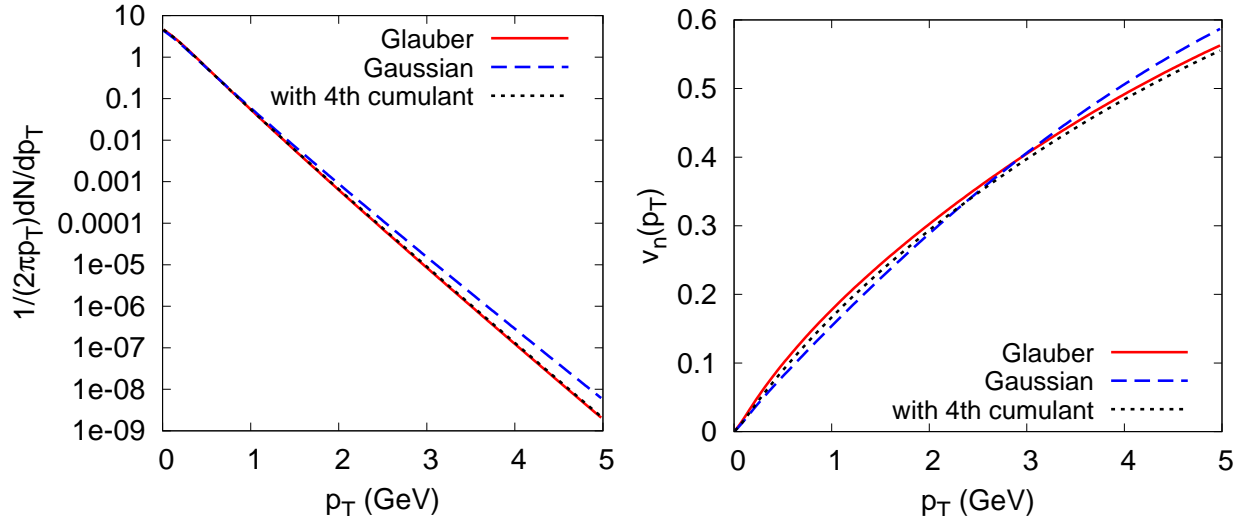


FIG. 7: (Color Online) (a) Spectra in the smooth (optical) Glauber model compared to the cumulant expansion. The coefficients of the Gaussian and fourth order cumulant expansions have been adjusted to reproduce  $\langle r^2 \rangle$ ,  $\langle r^2 \cos 2\phi \rangle$  and  $\langle r^4 \cos 2\phi \rangle$ ,  $\langle r^4 \cos 4\phi \rangle$  respectively. The total entropy of the cumulant expansion is also matched to the total entropy of the glauber distribution. (b) Elliptic flow in the Glauber model compared to the cumulant expansion.

between the Gaussian and the Glauber distribution. Taking the impact parameter to be  $b = 7.6$  fm, Fig. 7 compares the spectra and the elliptic flow for these two distributions. In the next approximation, the fourth cumulants to the Gaussian are adjusted as described in Section II D and Appendix A 2 to reproduce the  $\langle r^4 \rangle$ ,  $\langle r^4 \cos 2\phi \rangle$ , and  $\langle r^4 \cos 4\phi \rangle$  moments of the Glauber distribution. Fig. 7 shows that the cumulant expansion reproduces the response of the Glauber distribution in detail.

### III. TIME DEVELOPMENT OF THE RESPONSE

In the previous sections we introduced a set of initial conditions with definite triangularity and dipole asymmetry. In this section we will show how the hydrodynamic response to these cumulants develops in space and time. The point here is to understand the hydrodynamics without the complications of freezeout and a freezeout prescription.

To show how the dipole and triangular flow develop in time, we have generalized the discussion of elliptic flow given in Ref. [24]. The spatial anisotropy is characterized by the second moment

$$\epsilon_{2x} = -\frac{\langle r^2 \cos 2\phi \rangle}{\langle r^2 \rangle}, \quad (3.1)$$

which is a function of time in general. As the system expands, the spatial anisotropy decreases and the momentum anisotropy increases. The momentum anisotropy is traditionally

defined with  $\epsilon_{2p}$  :

$$\epsilon_{2p} \equiv \frac{\int d^2\mathbf{x} (T^{xx} - T^{yy})}{\int d^2\mathbf{x} (T^{xx} + T^{yy})} = \frac{\int d^2\mathbf{x} (e+p)u_r^2 \cos 2\phi_u}{\int d^2\mathbf{x} [(e+p)u_r^2 + 2p]}, \quad (3.2)$$

where  $u_r = \sqrt{(u^x)^2 + (u^y)^2}$  and  $\phi_u = \tan^{-1}(u^y/u^x)$ . This definition has its flaws since the numerators and denominators do not transform as components of a tensor under transverse boosts<sup>1</sup> [13]. An alternative definition is found by constructing an irreducible rank two tensor out of the momentum density  $T^{0i}$  and the flow velocity  $u^j$

$$T^{0(i}u^{j)} - \text{traces} \equiv \frac{1}{2} (T^{0i}u^j + T^{0j}u^i - \delta^{ij}T^{0l}u_l). \quad (3.3)$$

Then we define

$$\epsilon_{2p} = \frac{\int d^2\mathbf{x}\tau [T^{0(x}u^{x)} - \text{traces}]}{\int d^2\mathbf{x}\tau [T^{00}u^0]} = \frac{\int d^2\mathbf{x}\tau u^0 [(e+p)u_r^2 \cos 2\phi_u]}{\int d^2\mathbf{x}\tau u^0 [(e+p)u_r^2 + e]}, \quad (3.4)$$

which is almost the same as Eq. (3.2). For the triangularity and dipole asymmetry we define the (reducible) third rank tensor

$$T^{0(i}u^j u^{l)} = \frac{1}{3!} (T^{0i}u^j u^l + \text{perms}). \quad (3.5)$$

Then the traceless (or irreducible) tensor is used to define the momentum space triangular anisotropy

$$\epsilon_{3p} \equiv \frac{\int d^2\mathbf{x}\tau [T^{0(x}u^x u^{x)} - \text{traces}]}{\int d^2\mathbf{x}\tau [T^{00}u^0 u^0]} = \frac{\int d^2\mathbf{x}\tau u^0 [(e+p)u_r^3 \cos 3\phi_u]}{\int d^2\mathbf{x}\tau [T^{00}u^0 u^0]}, \quad (3.6)$$

and the trace is used to define momentum space dipole asymmetry

$$\epsilon_{1p} \equiv \frac{\int d^2\mathbf{x}\tau [\delta_{ji}T^{0(x}u^j u^{l)}]}{\int d^2\mathbf{x}\tau [T^{00}u^0 u^0]} = \frac{\int d^2\mathbf{x}\tau u^0 [(e+p)u_r^3 \cos \phi_u]}{\int d^2\mathbf{x}\tau [T^{00}u^0 u^0]}. \quad (3.7)$$

Armed with these definitions, Fig. 8 illustrates the development of the triangular flow and the dipole asymmetry as a function of time. As is familiar from studies of the elliptic flow [17, 24], the spatial anisotropy decreases leading to a growth of the momentum space anisotropy. When the spatial anisotropy crosses zero, the growth of the momentum space anisotropy stalls. The figures also indicate that the elliptic flow, the dipole asymmetry, and the triangularity all develop on approximately the same time scale,  $\tau \simeq \sqrt{\langle r^2 \rangle}/c_s$ .

Another important aspect of the flow is the transverse radial flow profile. To illustrate this profile we decompose the transverse flow velocity into harmonics:

$$u_r(r, \phi) = u_r^0(r) + 2u_r^{(1)}(r) \cos(\phi) + 2u_r^{(2)}(r) \cos(2\phi) + 2u_r^{(3)}(r) \cos(3\phi) + \dots \quad (3.8)$$

<sup>1</sup> This flaw is easily remedied by replacing  $d^2\mathbf{x}$  with the fluid three volume in the local rest frame  $d\Sigma_\mu u^\mu = d^2\mathbf{x}d\eta\tau u^0$ . The additional factor of  $u^0$  appears naturally below.

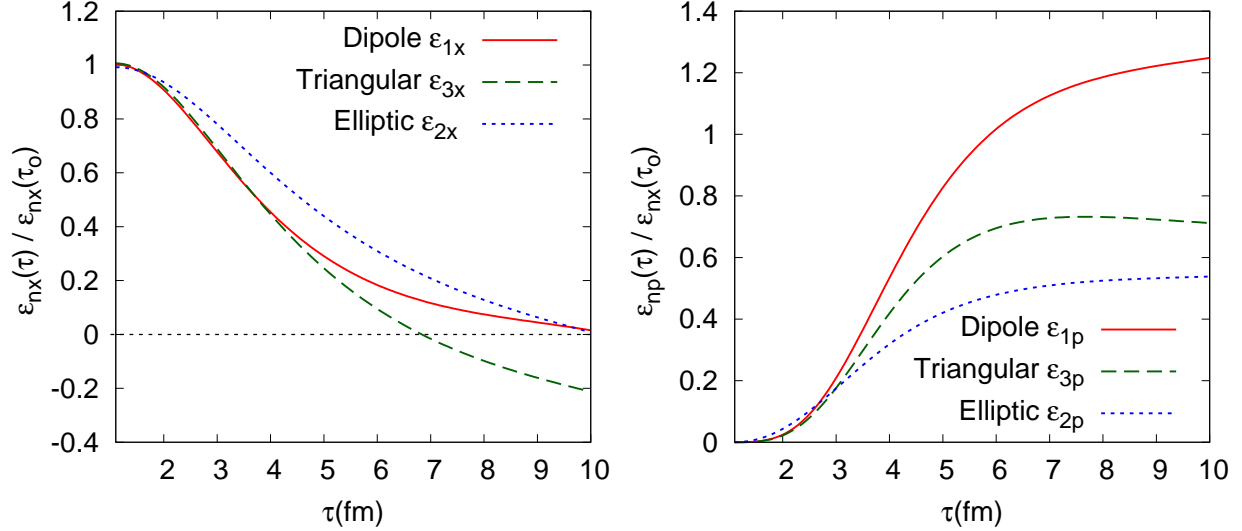


FIG. 8: (Color online) (a) The spatial anisotropy of the entropy distribution  $\epsilon_{1x}$ ,  $\epsilon_{2x}$ , and  $\epsilon_{3x}$  (see text) as a function of time for  $b = 7.6$  fm. (b) The momentum anisotropy  $\epsilon_{1p}$ ,  $\epsilon_{2p}$ , and  $\epsilon_{3p}$  (see text) as a function of time. The timescale in these figures should be compared to  $\sqrt{\langle r^2 \rangle}/c_s \simeq 5.4$  fm.

For a radially symmetric Gaussian distribution only the zero-th harmonic is present, and  $u_r^{(0)}$  shows a linearly rising flow profile. When the elliptic deformation is added the second harmonic also shows a linearly rising profile. Close to the origin this behavior can be understood with a linearized analysis of the acoustic waves. The flow velocity in an acoustic analysis is the gradient of a scalar function  $\Phi$  which can be expanded in harmonics:

$$\Phi(r, \phi) = \Phi^{(0)}(r) + 2\Phi^{(2)}(r) \cos 2\phi + \dots \quad (3.9)$$

If  $\Phi(r, \phi)$  is an analytic function of  $x$  and  $y$ , then  $\Phi^{(2)}$  must be quadratic for small  $r$ . Consequently the gradient of this function,  $u_r^{(2)}(r)$ , rises linearly at small  $r$ . Similarly, the triangular deformation  $\Phi^{(3)}(r)$  should be cubic at small  $r$  and the flow profile  $u_r^{(3)}$  should be quadratic. These features are borne out by our numerical work as exhibited in Fig. 9. Fig. 9 also shows the flow profile of the first harmonic which results from an initial dipole asymmetry. The first harmonic shows a negative slope at small  $r$  followed by a quadratically rising profile at larger  $r$ .

As seen from Fig. 9, the triangular and dipolar flows are biased towards the edge of the nucleus. In the next section we will see that due to this bias  $v_1$  and  $v_3$  are more sensitive to the freezeout prescription than  $v_2$ .

#### IV. PARTICLE SPECTRA: $v_1(p_T)$ AND $v_3(p_T)$

Having illustrated the essential features of the hydrodynamic response, we will compute the particle spectra associated with these flows. As discussed above, the analysis is limited to a classical massless ideal gas. We will follow the time honored, but poorly motivated

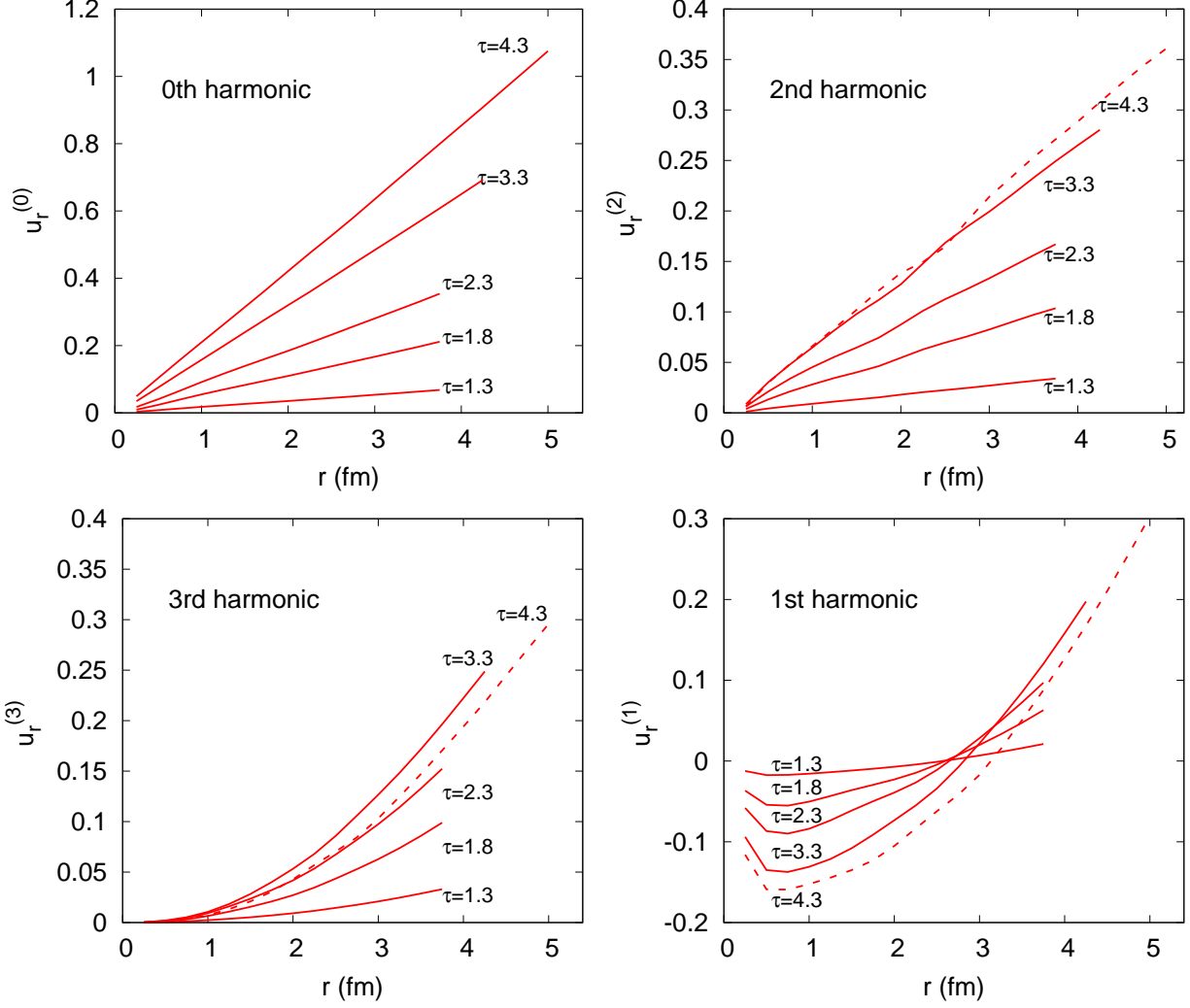


FIG. 9: (a) The zeroth harmonic of the flow profile (see Eq. 3.8) for the radially symmetric Gaussian adopted in this work. The root mean square radius of the Gaussian is adjusted to reproduce an impact parameter of 7.6 fm. (b) The second harmonic of the flow profile for an elliptic perturbation. (c) The third harmonic of the flow profile for a triangular perturbation (d) The first harmonic of the flow profile for a distribution with a net dipole asymmetry. The deformations  $\epsilon_1, \epsilon_2$  and  $\epsilon_3$  are all set to 0.1.

prescription of specifying a freezeout temperature or a freezeout entropy density. Freezeout temperatures in full hydrodynamic simulations with a Hadronic Resonance Gas (HRG) range from  $T = 160$  MeV to  $T = 120$  MeV [13, 18]. The total initial entropy and initial volume used in our massless ideal gas simulations were taken to be the similar to the total entropy and initial volume used in these full hydrodynamic simulations. The final freezeout volume of our massless-gas simulation is also taken to be similar to the final freezeout volume of these full simulations. Since entropy is conserved, this can be accomplished by adjusting the freezeout entropy density of the massless gas so that the entropy density equals the HRG



Hadron Gas $T_{\text{fo}}$	Hadron Gas $s_{\text{fo}}$	Massless Gas $T_{\text{fo}}$
130 MeV	$4.34 \text{ fm}^{-3}$	71 MeV
150 MeV	$1.87 \text{ fm}^{-3}$	96 MeV
170 MeV	$0.77 \text{ fm}^{-3}$	127 MeV

TABLE I: Table of freezeout temperatures used in this work. The first two columns show freezeout temperatures and the corresponding entropy densities of a Hadron Resonance Gas (HRG) EOS. The last column shows the freezeout temperatures where the massless gas EOS used in this work attains the corresponding HRG entropy density.

entropy density for a specified HRG freezeout temperature. Experience has shown that this is a fair way to compare different equations of state. Rather than quoting the actual freezeout temperature of the massless gas EOS, we will simply quote the corresponding HRG freezeout temperature. Thus  $T \Leftrightarrow 170 \text{ MeV}$  means that the actual freezeout temperature is such that the entropy density of a massless gas is equal to the entropy density of the HRG at  $T = 170 \text{ MeV}$ . Table I shows a set of temperatures and entropy densities in a HRG model and the corresponding freezeout temperatures for the massless gas equation of state.

Fig. 10 shows the momentum anisotropies as a function of time, and marks when the average entropy density of the system reaches a specified freezeout entropy density. Specifically, the lines indicate when  $\langle s \rangle$  in the notation of Eq. (2.6) falls below the freezeout entropy density indicated in Table I. We see that for  $T_{\text{fo}} \Leftrightarrow 170 \text{ MeV}$  the triangular and dipole flows are still developing, while for  $T_{\text{fo}} \Leftrightarrow 130 \text{ MeV}$  the flows are almost fully developed.

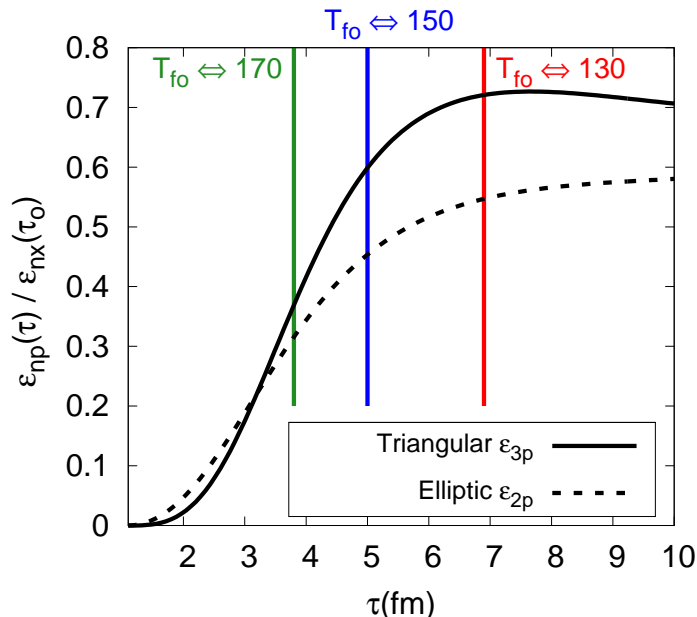


FIG. 10: Evolution of the momentum anisotropy as a function of time at an impact parameter of  $b = 7.6 \text{ fm}$ . The lines indicate when the average entropy density  $\langle s \rangle$  falls below the freezeout entropy density specified by the the temperatures  $T \Leftrightarrow 130, 150, 170 \text{ MeV}$ .

Once the freezeout surface is specified the particle spectra are computed using the Cooper-Frye formula

$$(2\pi)^3 E \frac{dN}{d^3\mathbf{p}} = \int_V p^\mu dV_\mu f_o(-P \cdot U(X)), \quad (4.1)$$

where  $f_o(E) = g \exp(-E/T(X))$  is the distribution function of a classical massless gas. (The notation here follows the review article [13].) Using this formula we compute the particle spectra and determine the associated harmonics  $v_1$ ,  $v_2$  and  $v_3$ . For each impact parameter we determine the root-mean square radius and the total entropy from an optical Glauber model; then the Gaussian parameters are adjusted to reproduce these Glauber quantities; finally the simulation is run to the freezeout entropy density and the harmonics are computed. Fig. 11 shows how the harmonics depend on centrality and the freezeout temperature.

Examining Fig. 11 we see that  $v_1$ ,  $v_2$  and  $v_3$  are roughly independent of centrality. However, it must be borne in mind that in a more complete simulation, the total entropy per participant is also a function of centrality and this could change the result. Here the entropy per participant is constant. Generally the freezeout criterion is also a function of centrality and this could give a substantial shape to these curves in a final simulation. Finally, when viscosity is included the triangularity is also a more complicated function of centrality [14]. This will be explored elsewhere [21].

Fig. 12 shows how these harmonics depend on  $p_T$ .  $v_2(p_T)$  and  $v_3(p_T)$  show a characteristic linear rise with  $p_T$  that is a consequence of a strong radial flow [25–28]. Indeed examining the thermal distribution with constant temperature, we have

$$e^{P \cdot U/T} = e^{-E_{\mathbf{p}} U^\tau / T} e^{p_T / T} u_r(r, \phi) \cos(\phi_{\mathbf{p}} - \phi_u), \quad (4.2)$$

$$\simeq e^{-E_{\mathbf{p}} / T} e^{p_T / T} u_r^{(0)}(r) \cos(\phi_{\mathbf{p}} - \phi) \\ \times \left[ 1 + \frac{2p_T}{T} u_r^{(2)}(r) \cos(2\phi) \cos(\phi_{\mathbf{p}} - \phi) + \frac{2p_T}{T} u_r^{(3)}(r) \cos(3\phi) \cos(\phi_{\mathbf{p}} - \phi) + \dots \right]. \quad (4.3)$$

Here  $E_{\mathbf{p}}$  is the energy,  $\phi_{\mathbf{p}}$  is the particles azimuthal angle; we have adopted a non-relativistic approximation  $U^\tau \simeq 1$  and assumed that the flow is approximately radial,  $\phi_u \simeq \phi$ . Further, we have neglected  $u_r^{(1)}$  in this discussion. Unless the momentum angle equals the spatial angle  $\phi_{\mathbf{p}} \simeq \phi$ , the thermal distribution is strongly suppressed by the leading Boltzmann factor. Thus, we arrive at a form which illustrates the linear rise of rise of  $v_n(p_T)$  with  $p_T$

$$e^{P \cdot U/T} \simeq e^{-E_{\mathbf{p}} / T} e^{p_T / T} u_r^{(0)}(r) \left[ 1 + \frac{2p_T}{T} u_r^{(2)}(r) \cos(2\phi_{\mathbf{p}}) + \frac{2p_T}{T} u_r^{(3)}(r) \cos(3\phi_{\mathbf{p}}) + \dots \right]. \quad (4.4)$$

Examining Fig. 12, we see that  $v_1(p_T)$  also displays a similar linearly rising trend at higher  $p_T$  after an initial dip.

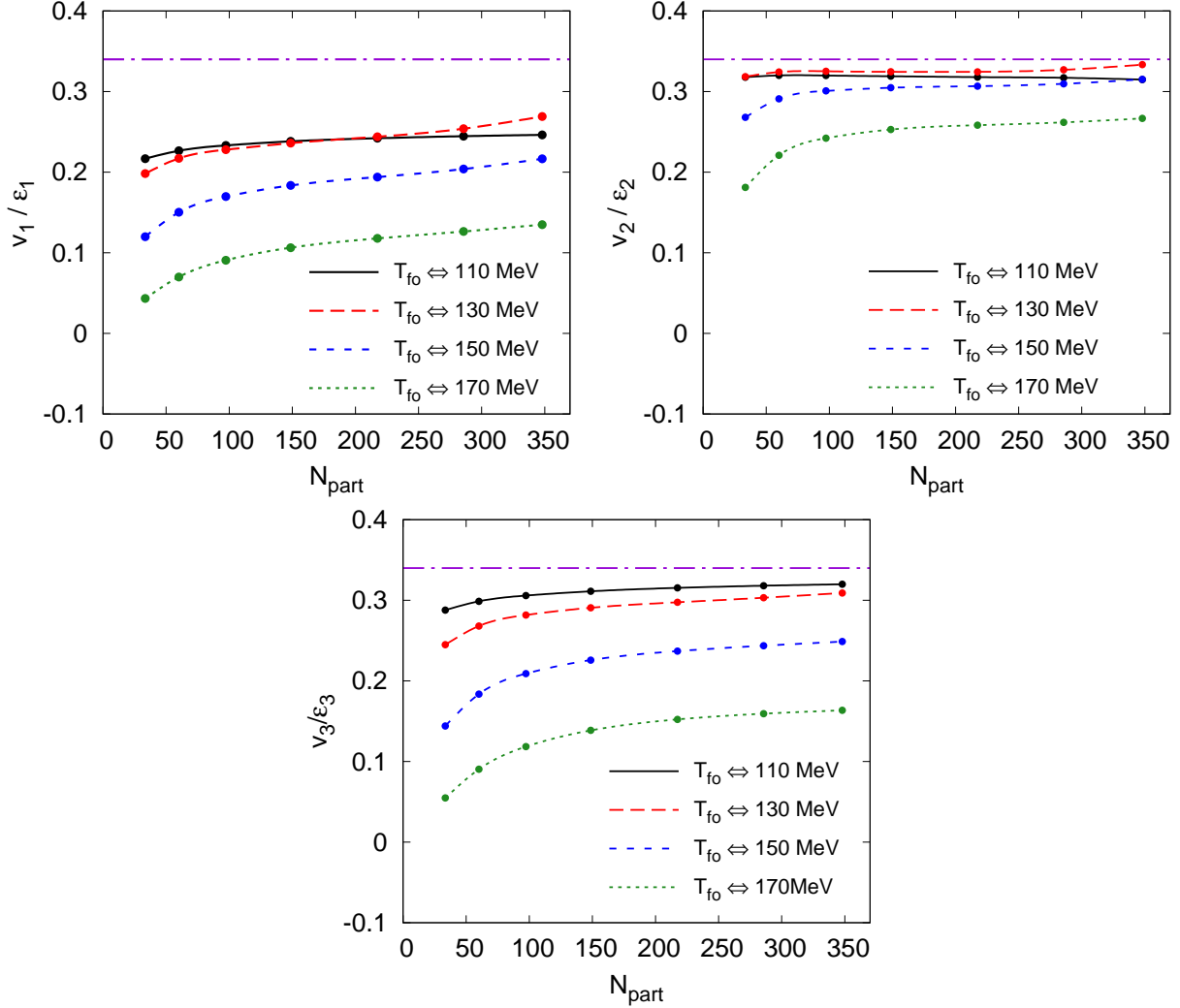


FIG. 11:  $v_1$ ,  $v_2$  and  $v_3$  per unit anisotropy as a function of  $N_{\text{part}}$  for different freezeout temperatures. The anisotropy parameters are all 0.1 in the actual simulations.

## V. FURTHER PREDICTIONS AND COMPARISON WITH OTHER WORKS.

### A. Further predictions

Fig. 11 and Fig. 12 show the response of the hydrodynamic system to the deformations. Certainly it is premature to compare the current calculation to data. For instance, the effect of viscosity, resonance decays, and a lattice-based equation of state have not been included. These reality factors will reduce the response. Nevertheless, in order to keep the final goal clearly in sight, we will provisionally compare the current calculation to the Alver Roland fit [1] of STAR inclusive two particle correlations [29]. Further, we will suggest a number of additional observables which can confirm the geometric nature of the measured two particle correlations.

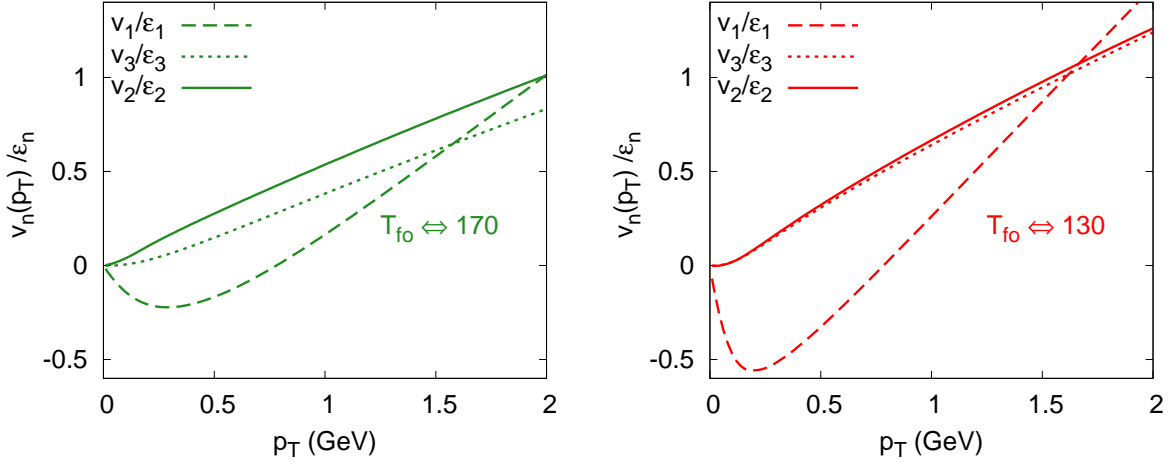


FIG. 12:  $v_n(p_T)$  for two different freezeout temperatures as described in Table I. The root mean square radius of the initial Gaussian corresponds to a radius of  $b = 7.6$  fm

The average over glauber configurations at fixed  $N_{\text{part}}$  is denoted with double brackets  $\langle\langle \dots \rangle\rangle$ . Then the two particle angular correlation function can be expanded in a Fourier series:

$$\left\langle\left\langle \frac{dN_{\text{pairs},\alpha\beta}}{d\phi_\alpha d\phi_\beta} \right\rangle\right\rangle = \langle\langle N_{\text{pairs},\alpha\beta} \rangle\rangle \left( 1 + \sum_n 2V_{n\Delta} \cos(n\phi_\alpha - n\phi_\beta) \right). \quad (5.1)$$

The particle labels  $\alpha$  and  $\beta$  could denote distinct particle types or  $p_T$  bins for example. Following Alver and Roland we will approximate the two particle correlation with the disconnected component. The yield of particle type  $\alpha$  for a fixed Glauber configuration is

$$\frac{dN_\alpha}{d\phi_\alpha} = \frac{N_\alpha}{2\pi} \left[ 1 + 2\frac{v_{1\alpha}}{\epsilon_1} \epsilon_1 \cos(\phi_\alpha - \psi_{1,3}) + 2\frac{v_{2\alpha}}{\epsilon_2} \epsilon_2 \cos(2\phi_\alpha - 2\Psi_{PP}) + 2\frac{v_{3\alpha}}{\epsilon_3} \epsilon_3 \cos(3\phi_\alpha - 3\psi_{3,3}) \right], \quad (5.2)$$

where we have assumed that the response is linearly proportional to the deformation. Then the two particle correlation function is approximated as

$$\left\langle\left\langle \frac{dN_{\text{pairs},\alpha\beta}}{d\phi_\alpha d\phi_\beta} \right\rangle\right\rangle \simeq \left\langle\left\langle \frac{dN}{d\phi_\alpha} \frac{dN}{d\phi_\beta} \right\rangle\right\rangle \simeq \frac{N_\alpha N_\beta}{(2\pi)^2} \left[ 1 + \sum_n 2 \left( \frac{v_{n\alpha} v_{n\beta}}{\epsilon_n^2} \right) \langle\langle \epsilon_n^2 \rangle\rangle \cos(n(\phi_\alpha - \phi_\beta)) \right]. \quad (5.3)$$

Here and below we have tacitly assumed that the multiplicity fluctuations at fixed  $N_{\text{part}}$  are negligible. If this is not the case then one has the following replacements in Eq. (5.3)

$$N_\alpha N_\beta \rightarrow \langle\langle N_\alpha N_\beta \rangle\rangle \quad \langle\langle \epsilon_n^2 \rangle\rangle \rightarrow \frac{\langle\langle N_\alpha N_\beta \epsilon_n^2 \rangle\rangle}{\langle\langle N_\alpha N_\beta \rangle\rangle}. \quad (5.4)$$

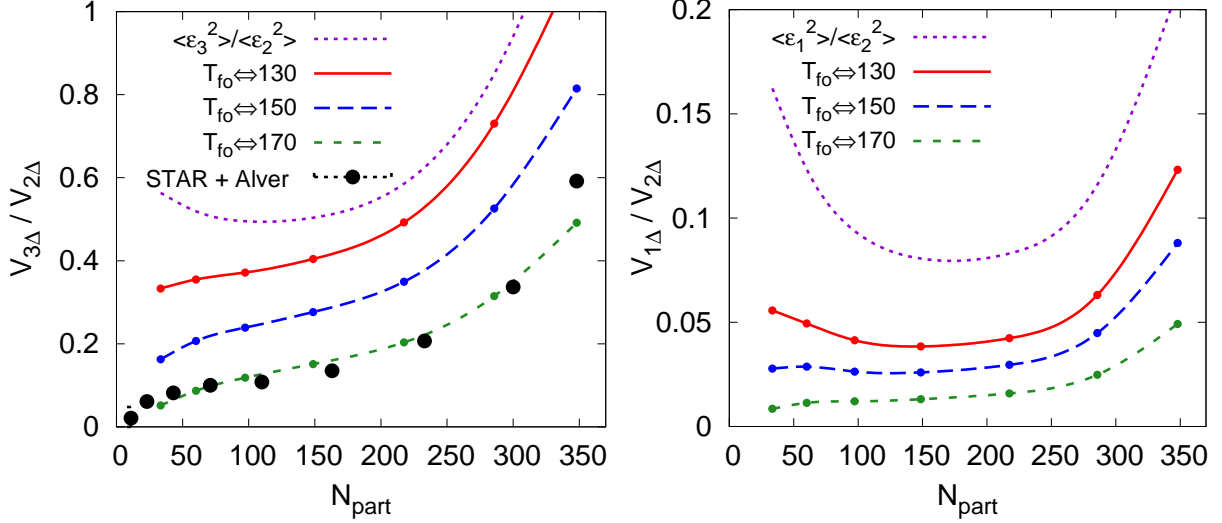


FIG. 13: Fourier components of the two particle correlation function as a function of  $N_{\text{part}}$  relative to the quadrupole component. (a) The triangularity component compared to the Alver Roland fit [1] of STAR inclusive two particle correlation functions [29]. (b) The dipole component relative to the quadrupole component; note that the scales differ between (a) and (b).

Given the parameterizations in Eq. (5.1) and Eq. (5.3), the response functions in Fig. 11 make a definite prediction for the different Fourier components  $V_{n\Delta}$ . The elliptic flow is too large in the ideal massless gas model considered here. We will therefore simply plot the ratios of the different Fourier components as was done in the Alver and Roland paper. Using the response functions in Fig. 11, and the Glauber estimates for  $\langle \langle \epsilon_3^2 \rangle \rangle / \langle \langle \epsilon_2^2 \rangle \rangle$ , Fig. 13(a) compares the strength of the triangular component to the quadrupole component. The ideal hydrodynamic prediction (with a massless ideal gas EOS) is generally too large and fairly sensitive to the freezeout temperature. This sensitivity reflects the fact that the triangular flow develops further towards the edge of the nucleus. Fig. 13(b) compares the dipole component to the quadrupole component. The dipole component is a factor of eight smaller than the quadrupole component. This is a reflection of the fact that  $\epsilon_1$  is small, and the fact that  $v_1(p_T)/\epsilon_1$  is positive and negative. The dipolar flow is also sensitive to the details of freezeout.

Next we wish to determine the general form of the two particle correlation function with respect to the participant plane  $\Psi_{PP}$

$$\left\langle \left\langle \frac{dN_{\text{pairs},\alpha\beta}}{d\phi_1 d\phi_2} \right\rangle \right\rangle_{\Psi_{PP}} \simeq \left\langle \left\langle \frac{dN_\alpha}{d(\phi_\alpha - \Psi_{PP})} \frac{dN_\beta}{d(\phi_\beta - \Psi_{PP})} \right\rangle \right\rangle_{\Psi_{PP}}. \quad (5.5)$$

Inserting Eq. (5.2) into Eq. (5.5) and averaging over Glauber configurations several terms appear. In Section B we identified the principle correlations that exist between the angles  $\psi_{1,3}, \psi_{3,3}$  and  $\Psi_{PP}$ . Namely, the only significant Fourier expectation values are  $\langle \cos(2\psi_{1,3} - 2\Psi_{PP}) \rangle$  (as determined by the coefficient  $A$  in Eq. (2.36)), and  $\langle \cos(\psi_{1,3} - 3\psi_{3,3} + 2\Psi_{PP}) \rangle$  (as determined by the coefficient  $B_0$  in Eq. (2.43)). With the

assumption that these are the only significant fourier expectation values at third order, the form of the two particle correlation function with respect to participant plane becomes:

$$\begin{aligned}
\left\langle\left\langle\frac{dN_{\text{pairs},\alpha\beta}}{d\phi_\alpha d\phi_\beta}\right\rangle\right\rangle &\simeq \frac{N_\alpha N_\beta}{(2\pi)^2} \left[ 1 + \sum_n 2 \left( \frac{v_{n\alpha} v_{n\beta}}{\epsilon_n^2} \right) \langle\langle \epsilon_n^2 \rangle\rangle \cos(n\phi_\alpha - n\phi_\beta) \right. \\
&+ 2 \frac{v_{2\alpha}}{\epsilon_2} \langle\langle \epsilon_2 \rangle\rangle \cos(2\phi_\alpha - 2\Psi_{PP}) \\
&+ 2 \frac{v_{2\alpha} v_{2\beta}}{\epsilon_2^2} \langle\langle \epsilon_2^2 \rangle\rangle \cos(2\phi_\alpha + 2\phi_\beta - 4\Psi_{PP}) \\
&+ 2 \frac{v_{1\alpha} v_{1\beta}}{\epsilon_1^2} \langle\langle \epsilon_1^2 \cos(2\psi_{1,3} - 2\Psi_{PP}) \rangle\rangle \cos(\phi_\alpha + \phi_\beta - 2\Psi_{PP}) \\
&+ 2 \frac{v_{1\alpha} v_{3\beta}}{\epsilon_1 \epsilon_3} \langle\langle \epsilon_1 \epsilon_3 \cos(\psi_{1,3} - 3\psi_{3,3} + 2\Psi_{PP}) \rangle\rangle \cos(\phi_\alpha - 3\phi_\beta + 2\Psi_{PP}) \\
&\left. + \alpha \leftrightarrow \beta \right]. \tag{5.6}
\end{aligned}$$

The symmetrization with respect to  $\alpha$  and  $\beta$  applies to all terms in this expression which are not already symmetric, *e.g.*  $\cos(2\phi_\alpha - 2\Psi_{PP})$ . We will discuss this expression line by line. The first three lines are not particularly novel: The first line is independent of the reaction plane angle  $\Psi_{PP}$ . The next two lines reflect the underlying elliptic flow and would normally be subtracted in a flow subtracted two particle correlation function.

The fourth line contains the first novel feature. This term arises because the dipole asymmetry is preferentially oriented out plane, leading to a net  $v_1$  out of plane. Fig. 14(a) shows the correlation function  $\langle\cos(\phi_\alpha + \phi_\beta - 2\Psi_{PP})\rangle$  as a function of centrality. Recently, the STAR collaboration measured a similar expectation value, but divided correlation function into the different possible charge components (*i.e.* ++, +-, --) in order to investigate the possibility of local parity violation in heavy ion collisions [30–32]. Fig. 14(b) shows the measured STAR correlations. The measured correlation is the same order of magnitude as the out of plane flow found in this work. However many aspects of the out of plane dipole flow (*e.g.* the  $p_T$  dependence and most importantly the charge dependence) do not agree with the measured correlation. Thus the STAR measurements can constraint the geometric fluctuations reported here. This will be investigated in future work.

A second novel feature expressed by the two particle correlation function with respect to reaction plane is recorded by the 5th line of Eq. (5.5). It shows that hydrodynamics, together with the geometric fluctuations of the Glauber model makes a definite prediction for the angular correlation

$$\langle\langle \cos(\phi_\alpha - 3\phi_\beta + 2\Psi_{PP}) \rangle\rangle. \tag{5.7}$$

Taking  $\alpha$  to label all the particles in a definite  $p_T$  bin and  $\beta$  all the particles, this definite prediction reads

$$\langle\langle \cos(\phi_\alpha - 3\phi_\beta + 2\Psi_{PP}) \rangle\rangle = \frac{v_1(p_T)}{\epsilon_1} \frac{v_3}{\epsilon_3} \langle\langle \epsilon_1 \epsilon_3 \cos(\psi_{1,3} - 3\psi_{3,3} + 2\Psi_{PP}) \rangle\rangle. \tag{5.8}$$

This result is illustrated in Fig. 15 and is based on the Glauber analysis in Fig. 6 and the response functions calculated in Fig. 12. Another way to probe this same correlation is the following. Experimentally, the participant plane  $\Psi_{PP}$  is traditionally estimated by using

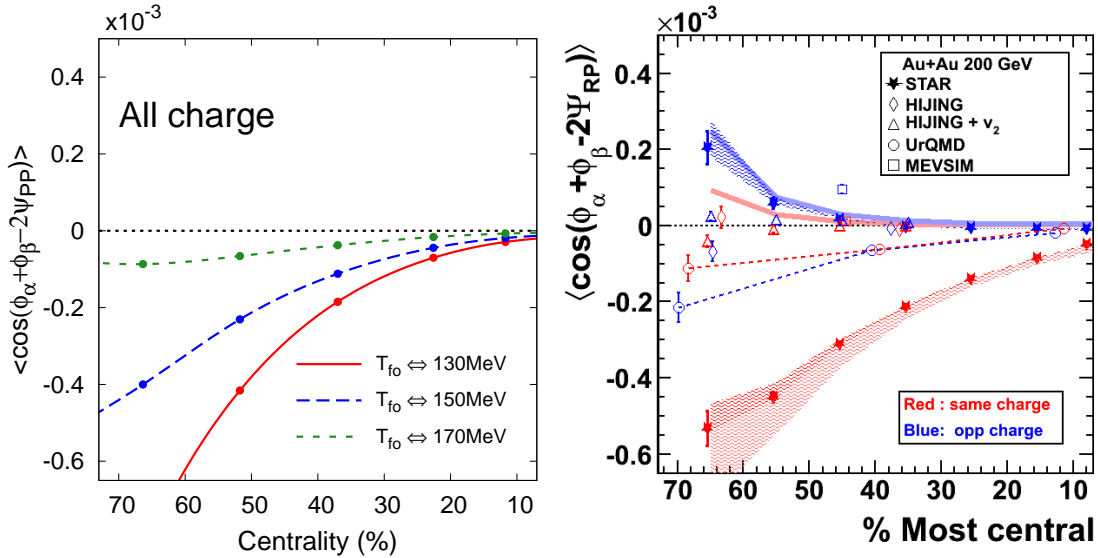


FIG. 14: (a) The expectation value  $\langle \cos(\phi_\alpha + \phi_\beta - 2\Psi_{PP}) \rangle$  as predicted by hydrodynamics, where  $\alpha$  and  $\beta$  label all particles. (b) The charge asymmetry with respect to reaction plane  $\langle \cos(\phi_\alpha + \phi_\beta - 2\Psi_R) \rangle$  as measured by the STAR collaboration [30, 31]. Here  $\alpha$  and  $\beta$  label  $++$ ,  $+-$ , or  $--$ . The hydrodynamic prediction does not explain the charge asymmetry.

the standard  $Q$  vector method, or the Yang-Lee zero generalization of this idea [33]. These same methods can be used to determine the triangularity event plane  $\psi_{3,3}$  without significant modifications [34]. The strong correlation between the dipole, triangular, and participant planes implies that the knowledge of  $\psi_{3,3}$  and  $\Psi_{PP}$  determines the dipole event plane  $\psi_{1,3}$  at least statistically. The most probable orientation is given by Eq. (2.45) and is repeated here for convenience

$$\psi_{1,3}^{\text{mp}} = 3\psi_{3,3} - 2\Psi_{PP} - \pi.$$

Thus, the  $v_1$  associated with the dipole asymmetry can be determined by measuring the expectation value

$$\langle\langle \cos(\phi - \psi_{1,3}^{\text{mp}}) \rangle\rangle. \quad (5.9)$$

Essentially this correlation is a  $v_1$  with an extra twist to take out the shifting orientations of the dipole and triangular event planes – see Fig. 5.

## B. Discussion and comparison with other works

We hope that the cumulant expansion presented in Section II organizes and formalizes the study of fluctuations in heavy ion collisions. The convergence of the cumulant expansion is really quite good as illustrated in Fig. 7. At third order in the cumulant expansion there are two additional terms, the triangularity  $\langle r^3 \cos 3(\phi - \psi_{3,3}) \rangle$ , and the dipole asymmetry  $\langle r^3 \cos(\phi - \psi_{1,3}) \rangle$ .

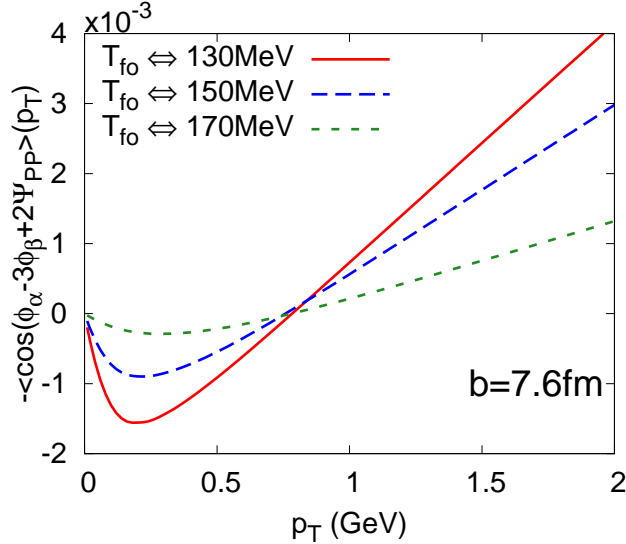


FIG. 15: A hydrodynamic prediction for the expectation value  $\langle \cos(\phi_\alpha - 3\phi_\beta + 2\Psi_{PP}) \rangle$  which reflects the correlation between the dipole, triangular, and elliptic event planes. Here  $\alpha$  labels all particles in a given  $p_T$  bin and  $\beta$  labels all particles.

Our numerical results for the triangularity  $v_3/\epsilon_3$  are similar to recently reported results [14, 15]. However,  $v_3$  (and  $v_1$ ) is significantly more sensitive to the freezeout dynamics. To understand this we studied the space time development of the triangularity (and dipole asymmetry) in Figs. 8 and 9. These figures indicate that the triangular flow develops on the same time scale as the elliptic flow. (A similar conclusion for the triangular flow was reached in Fig. 3 of Ref. [14] based on kinetic theory calculations.) However, there is an important difference between the elliptic flow and the dipole and triangular flows which has not been fully clarified previously. Specifically, the dipole and triangular moments of the transverse flow grow quadratically with radius,  $u_T^{(3)} \propto r^2$ , rather than linearly as is the case with elliptic flow,  $u_T^{(2)} \propto r$ . Consequently, edge effects can significantly reduce the dipole and triangular flows. Increasing the freezeout temperature cuts on the exterior region of the flow profile, and therefore  $v_1$  and  $v_3$  are more sensitive to the precise freezeout criterion (see Figs. 11 and 12). This unfortunate result may limit the usefulness of the dipole and triangular flows in determining the shear viscosity of the quark gluon plasma. Indeed the strong reduction of the  $v_3$  due to the shear viscosity [14, 15] is presumably largely due to the shear viscosity below  $T_c$ , though this conclusion requires further investigation.

We also investigated the dipole asymmetry,  $\langle r^3 \cos(\phi - \psi_{1,3}) \rangle$ . The dipole asymmetry appears to the same order in the gradient expansion and has not been studied previously to our knowledge. The dipole asymmetry is generally smaller than the triangularity since  $\epsilon_1$  is comparatively small. However,  $v_1/\epsilon_1$  is only marginally smaller than  $v_2/\epsilon_2$  and  $v_3/\epsilon_3$ . In non-central collisions the dipole asymmetry is strongly correlated with the triangularity and the reaction plane as is illustrated in Fig. 4 and explained in Fig. 5. We find that in non-central collisions the dipole asymmetry is preferentially out of plane leading to a  $v_1$  out of plane.



The size of the observed correlation is somewhat smaller than the observed correlations measured by the STAR collaboration and does not explain the charge asymmetry.

Finally, we noted that the strong correlation between the dipole asymmetry and the triangularity can be measured experimentally by measuring two particle correlations with respect to reaction plane. The final result is a hydrodynamic prediction for a curious correlator

$$\langle\langle \cos(\phi_\alpha - 3\phi_\beta + 2\Psi_{PP}) \rangle\rangle, \quad (5.10)$$

which is shown in Fig. 15. This average is similar to averages used to investigate the Chiral Magnetic Effect (CME) and is no more difficult to measure. The hydrodynamic prediction for Eq. (5.10) is several times larger than the correlation currently measured by the STAR collaboration,  $\langle \cos(\phi_\alpha + \phi_\beta - 2\Psi_{PP}) \rangle$ . Thus, the proposed measurement is feasible and important. If the predictions of Fig. 15 are confirmed it would validate the hydrodynamic and geometric nature of the measured two particle correlations. Further, given the off-diagonal nature of the proposed measurement, it will be difficult to reproduce this correlation with other mechanisms.

The current study neglected the effects of shear viscosity and resonance decays and used an ideal gas rather than a lattice based equation of state. Incorporating these important corrections is left for future work.

## Acknowledgments

We gratefully acknowledge useful discussions with Jean-Yves Ollitrault, Sergei Voloshin, and especially Edward Shuryak. This work is supported by an OJI grant from the Department of Energy DE-FG-02-08ER4154 and the Sloan Foundation.

## Appendix A: Details of the cumulant expansion and initial conditions

### 1. Formal expansion

Our goal is to determine the cumulants of the underlying distribution  $\rho(\mathbf{x})$  and to decompose these cumulants into irreducible tensors with respect to rotations around the  $z$  axis.

First we expand  $\rho(\mathbf{x})$  and its Fourier transform  $\rho(\mathbf{k})$  in a fourier series

$$\rho(\mathbf{x}) = \rho(r, \phi) = \rho_0(r) + 2 \sum_{n=1} \rho_n^c(r) \cos(n\phi) + 2 \sum_{n=1} \rho_n^s(r) \sin(n\phi), \quad (A1)$$

$$\rho(\mathbf{k}) = \rho(k, \phi_k) = \rho_0(k) + 2 \sum_{n=1} \rho_n^c(k) \sin(n\phi_k) + 2 \sum_{n=1}^{\infty} \rho_n^s(k) \sin(n\phi_k), \quad (A2)$$

where  $r, \phi, k, \phi_k$  are the magnitudes and azimuthal angles of  $\mathbf{x}$  and  $\mathbf{k}$  respectively. The relation between the  $\rho_n^{c,s}(k)$  and  $\rho_n^{c,s}(r)$  is established by substituting the identity

$$e^{i\mathbf{k}\cdot\mathbf{x}} = J_0(kr) + 2 \sum_{n=1}^{\infty} i^n J_n(kr) \cos(\phi - \phi_k) \quad (A3)$$

into the Fourier transform (Eq. (2.3)) and using elementary manipulations to obtain

$$\rho_n^{c,s}(k) = 2\pi \int r dr i^n J_n(kr) \rho_n^{c,s}(r). \quad (\text{A4})$$

Similarly, the generating function of cumulants is also given by a fourier series

$$W(\mathbf{k}) = W_0(k) + 2 \sum_n W_n^c(k) \cos(n\phi_k) + 2 \sum_n W_n^s(k) \sin(n\phi_k), \quad (\text{A5})$$

and each  $W_n^{c,s}(k)$  is expanded in  $k$  as described by equations Eqs. 2.16 and 2.22. Then we can expand both sides of the defining relation

$$\exp(W(\mathbf{k})) \equiv \rho(\mathbf{k}), \quad (\text{A6})$$

in a series expressions of the form  $k^m \cos(n\phi_k)$  and  $k^m \sin(n\phi_k)$ . In developing this expansion we use the series expansion of the Bessel function

$$J_\nu(z) = \left(\frac{1}{2}z\right)^\nu \sum_{k=0}^{\infty} (-1)^k \frac{\left(\frac{1}{4}z^2\right)^k}{k! \Gamma(\nu + k + 1)}, \quad (\text{A7})$$

and the series expansion of  $W_n^{c,s}(k)$ . Comparing identical powers of  $k^m \cos(n\phi_k)$  and  $k^m \sin(n\phi_k)$  we determine the  $W_{n,m}^{c,s}$  in terms of the moments of the underlying distribution. Through fifth order inclusive this comparison yields the following relations:

**0-th harmonic:**

$$W_{0,2} = \frac{1}{2} \langle r^2 \rangle, \quad (\text{A8})$$

$$W_{0,4} = \frac{3}{8} \left[ \langle r^4 \rangle - 2 \langle r^2 \rangle^2 - \underline{\langle r^2 \cos 2\phi \rangle^2} \right], \quad (\text{A9})$$

**2nd harmonic:**

$$W_{2,2}^c = \frac{1}{4} [\langle r^2 \cos 2\phi \rangle], \quad (\text{A10})$$

$$W_{2,4}^c = \frac{1}{4} [\langle r^4 \cos 2\phi \rangle - 3 \langle r^2 \rangle \langle r^2 \cos 2\phi \rangle], \quad (\text{A11})$$

$$W_{2,4}^s = \frac{1}{4} [\langle r^4 \sin 2\phi \rangle], \quad (\text{A12})$$

**4th harmonic:**

$$W_{4,4}^c = \frac{1}{16} \left[ \langle r^4 \cos 4\phi \rangle - 3 \underline{\langle r^2 \cos(2\phi) \rangle^2} \right], \quad (\text{A13})$$

$$W_{4,4}^s = \frac{1}{16} [\langle r^4 \sin 4\phi \rangle], \quad (\text{A14})$$

**1st harmonic:**

$$W_{1,3}^c = \frac{3}{8} [\langle r^3 \cos(\phi) \rangle] , \quad (\text{A15})$$

$$W_{1,3}^s = \frac{3}{8} [\langle r^3 \sin(\phi) \rangle] , \quad (\text{A16})$$

$$W_{1,5}^c = \frac{5}{16} \left[ \langle r^5 \cos(\phi) \rangle - 6 \langle r^2 \rangle \langle r^3 \cos \phi \rangle - \left( \langle r^2 \cos 2\phi \rangle \langle r^3 \cos 3\phi \rangle + 3 \langle r^3 \cos \phi \rangle \langle r^2 \cos 2\phi \rangle \right) \right] , \quad (\text{A17})$$

$$W_{1,5}^s = \frac{5}{16} \left[ \langle r^3 \sin(\phi) \rangle - 6 \langle r^2 \rangle \langle r^3 \sin \phi \rangle - \left( \langle r^2 \cos 2\phi \rangle \langle r^3 \sin 3\phi \rangle - 3 \langle r^3 \sin \phi \rangle \langle r^2 \cos 2\phi \rangle \right) \right] , \quad (\text{A18})$$

**3rd harmonic:**

$$W_{3,3}^c = \frac{1}{8} [\langle r^3 \cos(3\phi) \rangle] , \quad (\text{A19})$$

$$W_{3,3}^s = \frac{1}{8} [\langle r^3 \sin(3\phi) \rangle] , \quad (\text{A20})$$

$$W_{3,5}^c = \frac{5}{32} \left[ \langle r^5 \cos 3\phi \rangle - 4 \langle r^2 \rangle \langle r^3 \cos 3\phi \rangle - \underline{\langle r^3 \cos \phi \rangle \langle r^2 \cos 2\phi \rangle} \right] , \quad (\text{A21})$$

$$W_{3,5}^s = \frac{5}{32} \left[ \langle r^5 \sin 3\phi \rangle - 4 \langle r^2 \rangle \langle r^3 \sin 3\phi \rangle - \underline{\langle r^3 \sin \phi \rangle \langle r^2 \cos 2\phi \rangle} \right] , \quad (\text{A22})$$

**5th harmonic:**

$$W_{5,5}^c = \frac{1}{32} \left[ \langle r^5 \cos(5\phi) \rangle - \underline{10 \langle r^2 \cos 2\phi \rangle \langle r^3 \cos 3\phi \rangle} \right] , \quad (\text{A23})$$

$$W_{5,5}^s = \frac{1}{32} \left[ \langle r^5 \sin(5\phi) \rangle - \underline{10 \langle r^2 \cos 2\phi \rangle \langle r^3 \sin 3\phi \rangle} \right] . \quad (\text{A24})$$

Each coefficient has a simple interpretation. For instance,  $W_{0,2} = \frac{1}{2} \langle r^2 \rangle$  is simply the root mean square radius of the Gaussian. To classify corrections to the Gaussian, one should examine the difference between  $\langle r^4 \rangle$  and  $\langle r^2 \rangle^2$ ;  $W_{0,4} \simeq \frac{3}{8} \left[ \langle r^4 \rangle - 2 \langle r^2 \rangle^2 \right]$  is the required difference. The underlined terms (*i.e.*  $\underline{\langle r^2 \cos 2\phi \rangle^2}$  in the case  $W_{0,4}$ ) are of suppressed by a power of  $\epsilon^2$  and are therefore generally unimportant except in very peripheral collisions.

## 2. Fourier transform and regulating the cumulant expansion

After specifying the cumulants, the distribution is Fourier transformed to determine the initial entropy density in coordiante space. For simplicity we will discuss only a spherically symmetric Gaussian deformed by a small definite triangularity,  $W_{3,3}^c$ . In this case the Fourier transform of a distribution with  $W_{0,2}$  and small  $W_{3,3}^c$  ,

$$\rho(\mathbf{x}) = \int \frac{d^2 \mathbf{k}}{(2\pi)^2} e^{-i\mathbf{k} \cdot \mathbf{x}} e^{-\frac{k^2}{2} W_{0,2}} \left[ 1 + \frac{1}{3!} W_{3,3}^c (ik)^3 \cos 3\phi_k + \dots \right] , \quad (\text{A25})$$

yields with the definition of  $\epsilon_3$  in Eq. (2.30)

$$\rho(\mathbf{x}) = \left[ 1 + \frac{\langle r^3 \rangle \epsilon_3}{24} \left( \left( \frac{\partial}{\partial x} \right)^3 - 3 \left( \frac{\partial}{\partial y} \right)^2 \frac{\partial}{\partial x} \right) \right] \frac{e^{-\frac{r^2}{\langle r^2 \rangle}}}{\pi \langle r^2 \rangle}, \quad (\text{A26})$$

where  $\langle r^3 \rangle = 3\sqrt{\pi}/4 \langle r^2 \rangle^{3/2}$ . At large enough radius the correction term becomes large compared to the leading Gaussian. To regulate this term we replace the whole correction ( $\equiv X$ ) with

$$X \rightarrow C \tanh(X/C), \quad (\text{A27})$$

where  $C = 0.95$ . We have checked that the results are independent of the precise value of the constant  $C$ . The regulator here is not perfect as it (weakly) mixes different terms in the fourier expansion, but we have found this to be unimportant from a practical perspective, i.e. the  $v_2$  produced by this regulated  $\epsilon_3$  distribution is small. Another complication is that the input parameter  $\epsilon_3^{\text{input}}$  in the regulated version of Eq. (A26) does not actually equal the ‘‘true’’  $\epsilon_3$  of the initial distribution. In all figures we have divided by the true  $\epsilon_3 \equiv -\langle r^3 \cos(3\phi) \rangle$  rather than the input parameter  $\epsilon_3^{\text{input}}$ .

We can now specify precisely the initial conditions that are used for Fig. 11 and other results. At a given impact parameter we use the optical glauber model to calculate the distribution of participants the transverse plane with  $\sigma_{NN} = 40$  mb. In a traditional hydrodynamic simulation (such labeled by the ‘‘Glauber’’ curves in Fig. 7) the entropy density at an initial time  $\tau_0 = 1$  fm is

$$s(x, y, \tau_0) = \frac{C_s}{\tau_0} \frac{dN_p}{dx dy}, \quad (\text{A28})$$

where  $\frac{dN_p}{dx dy}$  is the number of participants per unit area. The value  $C_s = 15.9$  closely corresponds to the results of full hydrodynamic simulations [25, 35, 36] The equation of state that is used in this work is a classical massless ideal gas  $\mathcal{P} = 1/3 e$ . The relation between the temperature and energy density is  $e/T^4 \simeq 12.2$  which is the value for a two flavor ideal quark-gluon plasma. In the current simulations we calculate the total entropy and average squared radius  $\langle r^2 \rangle$  for glauber distribution. We then take a deformation  $\epsilon_3 \simeq 0.1$ , and use these parameters to initialize the regulated Gaussian described by Eq. (A26) and Eq. (A27). Finally, the simulation is run and the spectra are calculated leading to Fig. 2.

## Appendix B: Correlations in the Glauber model

The goal of this appendix is to motivate Eq. (2.39). A given distribution of participants is first characterized by the participant plane  $\Psi_{PP} \equiv \psi_{2,2}$  and we will assume that  $\epsilon_2$  is small. Then the probability distribution for  $\psi_{1,3}$  for fixed  $\Psi_{PP}$  is given by Eq. (2.36). For fixed  $\Psi_{PP}$  and  $\psi_{1,3}$  the probability distribution for  $\psi_{3,3}$  must be  $2\pi/3$  periodic. Measuring all angles with respect to participant plane and keeping only the first non-trivial term in the Fourier series we have

$$P(\psi_{3,3}|\psi_{1,3}\Psi_{PP}) = \frac{1}{2\pi} \left[ 1 + 2B \cos \left( 3(\psi_{3,3} - \Psi_{PP}) - (\phi^* - \Psi_{PP}) \right) \right]. \quad (\text{B1})$$

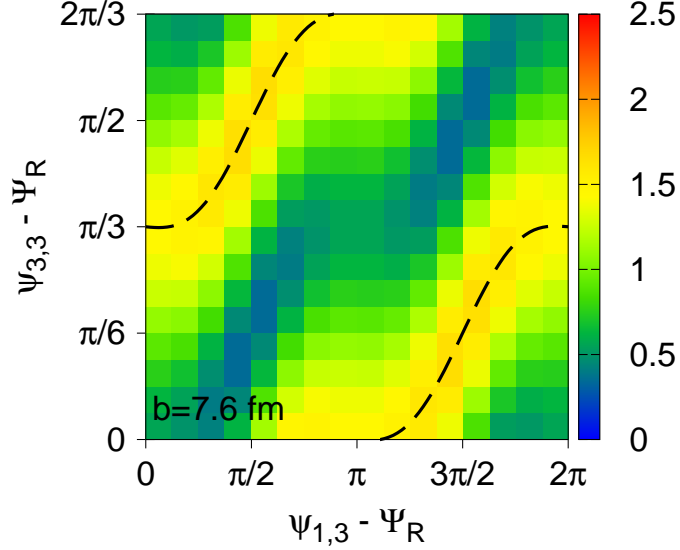


FIG. 16: A fit based on Eq. 2.39 to the the Glauber data exhibited in Fig. 4. The parameters are  $B_0 = 0.277(2)$ ,  $B_2 = 0.029(1)$ , and  $C = 0.532(7)$ . The normalization (*i.e.* the color scale) is arbitrary, but is the same as in Fig. 4.

The amplitude  $B$  and phase  $\phi^*$  are functions of  $\psi_{1,3} - \Psi_{PP}$ .

The amplitude  $B$  and the phase derivative can be expanded in a Fourier series

$$B = B_0 + 2B_2 \cos(2\psi_{1,3} - 2\Psi_{PP}) , \quad (\text{B2})$$

$$\frac{d\phi^*}{d\psi_{1,3}} = C_0 + 2C_2 \cos(2\psi_{1,3} - 2\Psi_{PP}) . \quad (\text{B3})$$

As the  $\psi_{1,3}$  increases by  $2\pi$ , the phase  $\phi^*$  must change by a multiple of  $2\pi$  to leave the conditional probability distribution invariant. The simplest possibility which qualitatively describes the trends illustrated in Fig. 4 and Fig. 5 is to take  $C_0 = 1$ . In a general fourier series of two variables other possibilities would be allowed, e.g.  $C_0 = 3$ . However such correlations turn out to be small in the Glauber model. Integrating Eq. (B3) we find

$$\phi = \psi_{1,3} + C_2 \sin(2\psi_{1,3} - 2\Psi_{PP}) + \text{const} \quad (\text{B4})$$

The constant required to reproduce Fig. 5 is  $\pi$ . The combination of Eqs. B1, B2, and B4 leads to the parameterization quoted in Eq. (2.39). In Eq. (2.39) we absorbed the constant phase  $\pi$  into the leading minus sign of  $B_0$  and  $B_2$  and changed the sign of  $C_2$  so that all coefficients are positive in the final fit. Fig. 16 shows a fit to the Monte Carlo Glauber shown in Fig. 5 at  $b = 7.6$  fm using this parameterization. The fit does capture most of the essential features, but fails to reproduce the sharpness of the correlation band.

Finally, we can estimate the scaling of these coefficients with the average elliptic eccentricity  $\langle\langle\epsilon_2\rangle\rangle$ . In a central collision  $B(\psi_{1,3}, \Psi_{PP})$  must vanish. This can be understood by examining Fig. 5 and recognizing that in a central collision there is no distinguishable difference between Position A and Position B. The coefficient of  $\cos(3\psi_{3,3} - \phi^* - \Psi_{PP})$  (*i.e.*  $B$ ) describes how phase between the triangular and the dipole planes changes from Position

A to Position B. This coefficient must vanish in central collisions where Position A and Position B are identical. Finally the coefficients  $B_2$  and  $C_2$  reflect the almond shape and must involve an additional power of  $\langle\langle\epsilon_2\rangle\rangle$  relative to  $C_0$  and  $B_0$ . With these remarks we arrive at the scalings given in Eq. (2.42).

- 
- [1] B. Alver and G. Roland, Phys. Rev. C **81**, 054905 (2010) [arXiv:1003.0194 [nucl-th]].
  - [2] J. Adams *et al.* [STAR Collaboration], Phys. Rev. Lett. **95**, 152301 (2005) [arXiv:nucl-ex/0501016].
  - [3] A. Adare *et al.* [PHENIX Collaboration], Phys. Rev. C **77**, 011901 (2008) [arXiv:0705.3238 [nucl-ex]].
  - [4] B. Alver *et al.* [PHOBOS Collaboration], Phys. Rev. Lett. **104**, 062301 (2010) [arXiv:0903.2811 [nucl-ex]].
  - [5] B. I. Abelev *et al.* [STAR Collaboration], Phys. Rev. C **80**, 064912 (2009) [arXiv:0909.0191 [nucl-ex]].
  - [6] D. Adamova *et al.* [CERES Collaboration], Phys. Lett. B **678**, 259 (2009) [arXiv:0904.2973 [nucl-ex]].
  - [7] B. I. Abelev *et al.* [STAR Collaboration], Phys. Rev. Lett. **102**, 052302 (2009) [arXiv:0805.0622 [nucl-ex]].
  - [8] J. Takahashi *et al.*, Phys. Rev. Lett. **103**, 242301 (2009) [arXiv:0902.4870 [nucl-th]].
  - [9] P. Sorensen, J. Phys. G **37**, 094011 (2010) [arXiv:1002.4878 [nucl-ex]].
  - [10] Z. W. Lin, C. M. Ko, B. A. Li, B. Zhang and S. Pal, Phys. Rev. C **72**, 064901 (2005) [arXiv:nucl-th/0411110].
  - [11] G. L. Ma *et al.*, Phys. Lett. B **641**, 362 (2006) [arXiv:nucl-th/0601012].
  - [12] S. Zhang *et al.*, Phys. Rev. C **76**, 014904 (2007) [arXiv:0706.3820 [nucl-th]].
  - [13] For a review and overview see: D. A. Teaney, arXiv:0905.2433 [nucl-th]. In “Quark-gluon plasma. Vol. 4,” editors R. C. Hwa and X. N. Wang.
  - [14] B. H. Alver, C. Gombeaud, M. Luzum and J. Y. Ollitrault, arXiv:1007.5469 [nucl-th].
  - [15] B. Schenke, S. Jeon and C. Gale, arXiv:1009.3244 [hep-ph].
  - [16] H. Petersen, G. Y. Qin, S. A. Bass and B. Muller, arXiv:1008.0625 [nucl-th].

- [17] J. Y. Ollitrault, Phys. Rev. D **46**, 229 (1992).
- [18] P. F. Kolb and U. W. Heinz, arXiv:nucl-th/0305084. In “Quark-gluon plasam. Vol. 3,” editors, R. C. Hwa and X. N. Wang.
- [19] B. Alver *et al.* [PHOBOS Collaboration], Phys. Rev. Lett. **98**, 242302 (2007) [arXiv:nucl-ex/0610037].
- [20] G. Y. Qin, H. Petersen, S. A. Bass and B. Muller, arXiv:1009.1847 [nucl-th].
- [21] Yan Li and D. Teaney, in progress.
- [22] B. Alver, M. Baker, C. Loizides and P. Steinberg, arXiv:0805.4411 [nucl-ex].
- [23] P. Staig and E. Shuryak, arXiv:1008.3139 [nucl-th].
- [24] P. F. Kolb, J. Sollfrank and U. W. Heinz, Phys. Rev. C **62**, 054909 (2000) [arXiv:hep-ph/0006129].
- [25] P. Huovinen, P. F. Kolb, U. W. Heinz, P. V. Ruuskanen and S. A. Voloshin, Phys. Lett. B **503**, 58 (2001) [arXiv:hep-ph/0101136].
- [26] N. Borghini and J. Y. Ollitrault, Phys. Lett. B **642**, 227 (2006) [arXiv:nucl-th/0506045].
- [27] A. P. Mishra, R. K. Mohapatra, P. S. Saumia and A. M. Srivastava, Phys. Rev. C **77**, 064902 (2008) [arXiv:0711.1323 [hep-ph]].
- [28] A. P. Mishra, R. K. Mohapatra, P. S. Saumia and A. M. Srivastava, Phys. Rev. C **81**, 034903 (2010) [arXiv:0811.0292 [hep-ph]].
- [29] B. I. Abelev *et al.* [STAR Collaboration], arXiv:0806.0513 [nucl-ex].
- [30] B. I. Abelev *et al.* [STAR Collaboration], Phys. Rev. Lett. **103**, 251601 (2009) [arXiv:0909.1739 [nucl-ex]].
- [31] B. I. Abelev *et al.* [STAR Collaboration], Phys. Rev. C **81**, 054908 (2010) [arXiv:0909.1717 [nucl-ex]].
- [32] D. Kharzeev, R. D. Pisarski and M. H. G. Tytgat, Phys. Rev. Lett. **81**, 512 (1998) [arXiv:hep-ph/9804221].
- [33] See the review: S. A. Voloshin, A. M. Poskanzer and R. Snellings, arXiv:0809.2949 [nucl-ex].
- [34] Sergei Voloshin, private communication.
- [35] D. Teaney, J. Lauret and E. V. Shuryak, arXiv:nucl-th/0110037. *ibid*, Phys. Rev. Lett. **86**, 4783 (2001)

- [36] P. F. Kolb, P. Huovinen, U. W. Heinz and H. Heiselberg, Phys. Lett. B **500**, 232 (2001)  
[arXiv:hep-ph/0012137].